

Real light curves of FK Comae Berenices: Dead end

L. Jetsu^{*}

Department of Physics, P.O. Box 64, FI-00014 University of Helsinki, Finland

Accepted XXX. Received YYY; in original form ZZZ

ABSTRACT

Recently, we presented a general model for the light curves of chromospherically active stars, where the observed light curve is interference of two real constant period light curves of long-lived starspots. In this first paper, we make six specific questions which undermine this argument, because it contradicts the current widely held views about the stellar surface differential rotation and the starspots. Our aim is to answer these six questions. We present evidence that the long-lived starspots of our general model have already been detected in the earlier surface imaging studies. The Lomb-Scargle power spectrum method analysis of the real and the simulated data of FK Com reveals that this method fails to detect the two real constant period light curves of our general model. *If* our model is valid, this method gives incompatible period, amplitude and minimum epoch estimates telling nothing about the real periods, the real amplitudes and the real minimum epochs of the two real light curves. This would mean that all earlier one-dimensional period analyses of the light curves of chromospherically active stars have given spurious results which have been widely and uncritically accepted since the discovery of the starspots in the year 1947. However, we arrive at a dead end, because we can not solve the real light curves of FK Com. In our second paper, we solve these real light curves with a new two-dimensional period finding method, prove the validity of our general model, and answer *all* six questions made in this first paper.

Key words: Methods: statistical – Methods: data analysis – Stars: starspots – Stars: activity – Stars: individual (FK Comae Berenices, HD117555)

1 INTRODUCTION

The ancient Egyptian papyrus Cairo 86637, which contains the calendar of lucky and unlucky days, is the oldest preserved historical document of the discovery of a variable star, Algol (Porceddu et al. 2008; Jetsu et al. 2013; Jetsu & Porceddu 2015; Porceddu et al. 2018). The Sun is also a variable star. The luminosity changes of Algol can be observed with naked eye, but those of the Sun can be reliably confirmed only with satellite observations (Willson & Hudson 1991; Radick et al. 2018). The oldest preserved drawing of a sunspot was made by John of Worcester in the year 1128 (Van Helden 1996). Schwabe (1844) discovered the eleven years cycle in the number of sunspots. The Zeeman effect caused by the solar magnetic field was discovered by Hale (1908), who also found out that this magnetic field is stronger in the sunspots.

Kron (1947) discovered the starspots in the light curves of the eclipsing binary AR Lacertae. He observed short-term light curve changes “within a few weeks to a few months”. FK Comae Berenices (HD 117555, FK Com) was among the

first late-type stars where the starspots were also discovered (Chugainov 1966). This chromospherically active single G4 giant (Strassmeier 2009) is the prototype of a class of variable stars, the FK Com class, defined by Bopp & Stencel (1981) as rapidly rotating single G–K giants. Only a few stars belonging to this class have been found (Puzin et al. 2014; Howell et al. 2016; Puzin et al. 2017). The members of this class may represent recently coalesced W UMa binaries (Webbink 1976; Bopp & Stencel 1981; Eggen & Iben 1989; Welty & Ramsey 1994).

The starspots on the surface of FK Com seem to concentrate on two long-lived active longitudes separated by 180 degrees, and undergo abrupt shifts between these longitudes. These shifts are called the flip-flop events (Jetsu et al. 1991, 1993). This phenomenon has also been observed in the chromospherically active binaries (e.g. Jetsu 1996, σ Gem). Hackman et al. (2013) applied the Kuiper method (hereafter the K-method) to the seasonal light curve minimum epochs of FK Com. This analysis gave the active longitude period $P_{\text{act}} = 2.^{\text{d}}401155 \pm 0.^{\text{d}}000092$. Numerous photometric studies of FK Com have been made (e.g. Korhonen et al. 2002; Oláh et al. 2006; Panov & Dimitrov 2007; Hackman et al. 2013). The starspot distribution of

* E-mail: lauri.jetsu@helsinki.fi

FK Com has also been mapped with the surface imaging methods (e.g. Korhonen et al. 1999, 2000, 2004, 2007, 2009; Hackman et al. 2013; Vida et al. 2015).

Jetsu et al. (2017) presented a general light curve model for the Chromospherically Active Binary Stars (hereafter CABS). They studied the long-term Mean Light Curve (hereafter MLC) of fourteen CABSs as a function of orbital phase, and also showed how their new model can be applied to the photometry of Chromospherically Active Single Star (hereafter CASS), like FK Com.

Jetsu et al. (2017, JHL = Jetsu, Henry, Lehtinen) made the following argument

- JHL-argument: “The *observed* light curves of chromospherically active binary and single stars are interference of two *real* constant period light curves of long-lived starspots. These constant periods are the non-stationary active longitude period P_{act} and the stationary rotation period $P_{\text{rot}} \approx P_{\text{orb}}$.”

At first sight, this JHL-argument would seem to contradict the current overwhelming observational evidence for stellar Surface Differential Rotation (hereafter SDR). There are two widely used observational methods for measuring stellar SDR (Strassmeier 2009, Sect. 7). In the first method, the rotation periods P_{rot} of starspots at different latitudes are measured from the Surface Images (hereafter the SI-method, e.g. Petit et al. 2004; Barnes et al. 2005; Collier Cameron 2007; Strassmeier 2009; Balona & Abedigamba 2016; Kóvári et al. 2017). The second method measures the range of the photometric rotation period $P_{\text{phot}} \approx P_{\text{rot}}$ changes in the Light Curves (hereafter the LC-method, e.g. Hall & Busby 1990; Hall 1991; Reinhold & Reiners 2013; Reinhold et al. 2013; Reinhold & Gizon 2015; Lehtinen et al. 2016; Distefano et al. 2016). There are numerous studies, where the SI-method and the LC-method give *different* SDR estimates even for the *same* individual star. For example, the SI-method study by Korhonen et al. (2000) indicated “solid body rotation” in FK Com, but photometric rotation period changes of about 3.1% were measured with the LC-method by Hackman et al. (2013, $Z \approx 0.0308$).

If the JHL-argument is true, then we must be able to answer at least five of the six undermining questions made below. The validity our argument does not depend on the 3rd question. On the contrary, the JHL-argument provides an answer to this question.

In our Abstract, we refer to these six specific questions:

- 1st question: Why have these two constant periods, the non-stationary active longitude period P_{act} and the stationary rotation period $P_{\text{rot}} \approx P_{\text{orb}}$ of the JHL-argument, *not* been detected in the surface images?
- 2nd question: Why have these two constant periods, the non-stationary active longitude period P_{act} and the stationary rotation period $P_{\text{rot}} \approx P_{\text{orb}}$ of the JHL-argument, *not* been detected in the light curves? Why are so *many different* $P_{\text{rot}} \approx P_{\text{phot}}$ periods *observed* in the light curves of the *same* star, if the photometric data contains only these two constant periods?
- 3rd question: Why do the surface images and the light curves give *different* surface differential rotation estimates even for the *same* individual star?

- 4th question: Hackman et al. (2013) applied the Kuiper method to the $t_{\text{min},1}$ light curve minima of FK Com. Does this kind of an analysis give an *unambiguous* estimate for the non-stationary active longitude period P_{act} of the JHL-argument?

- 5th question: The Kuiper method detects the non-stationary active longitude period P_{act} of the JHL-argument from the seasonal $t_{\text{min},1}$ light curve minima of chromospherically active binary stars (Jetsu et al. 2017) and single stars (Hackman et al. 2013). Why does this method *not* detect the stationary rotation period $P_{\text{rot}} \approx P_{\text{orb}}$ of the JHL-argument? The long-term mean light curves of chromospherically active binary stars in Jetsu et al. (2017) follow the stationary rotation period $P_{\text{rot}} \approx P_{\text{orb}}$ of the JHL-argument. Why do these long-term mean light curves *not* follow the non-stationary active longitude period P_{act} of the JHL-argument?

- 6th question: What explains the observed *abrupt* flip-flop events in the chromospherically active stars, if the long-lived starspots rotate with the two *regular constant* periods, the non-stationary active longitude period P_{act} and the stationary rotation period $P_{\text{rot}} \approx P_{\text{orb}}$?

In this first paper, we can not answer *all* these six questions. In our next second paper, we present a new period analysis method based on the JHL-argument, apply this method to the photometry of FK Com and give compact answer to *all* the above six questions (Jetsu 2018, hereafter PAPER II).

Our Appendix gives all abbreviations used in this paper.

2 DATA

We analyse the standard Johnson *V* photometry of FK Com published by Hackman et al. (2013). These observations were made with the “T7” and “Ph10” telescopes. We denote these separate samples of observations with TEL=1 (“T7”) and TEL=2 (“Ph10”). Hackman et al. (2013) stored them as two separate files into the CDS database. We analyse these two files separately, to avoid bias, as Hackman et al. (2013) also did. The accuracy of this photometry is between 0.^m004 and 0.^m008 in good photometric nights (Henry 1995; Strassmeier et al. 1997). All observations where the standard deviation of three measurements exceeds 0.^m020 are automatically discarded.

We discard $n = 68$ observations (Table 1). The number of remaining analysed observations is $n = 3807$.

The *isolated* first segment of TEL=2 data in Hackman et al. (2013) contains too few observations for reliable modelling, and it is discarded (Table 1: C=1, $n = 23$).

We divide the remaining data into seasonal segments (Table 2: SEG). These segment numbers are also used for the rest of the discarded data in Table 1.

Some *isolated* observations are discarded in the beginning or in the end of a few segments (Table 1: C=2, $n = 24$). These isolated observations would mislead the second order polynomial fits which are used to eliminate the changes of the mean brightness within segments (Sect. 3: Eq. 1). The fraction of all *isolated* discarded observations, $n = 47$, is 1.2% in all data.

We use a sliding window to identify the first group of *outliers*. The mean (m) and the standard deviation (s) is computed for all observations that are within $t \pm 30$ days

Table 1. Discarded data. Observing time (HJD), magnitude (V), telescope (TEL), segment (SEG) and discarding criterion (C)

HJD	V	TEL	SEG	C
2449876.7555	8.213	2	–	1
2449878.6786	8.109	2	–	1
2449882.6775	8.192	2	–	1
2449883.6783	8.158	2	–	1
2449883.7229	8.155	2	–	1
2449886.7003	8.309	2	–	1
2449886.7292	8.304	2	–	1
2449887.6784	8.180	2	–	1
2449888.6833	8.203	2	–	1
2449891.6809	8.346	2	–	1
2449893.6815	8.260	2	–	1
2449894.6718	8.250	2	–	1
2449896.6696	8.330	2	–	1
2449898.6701	8.308	2	–	1
2449900.6693	8.217	2	–	1
2449901.6691	8.289	2	–	1
2449902.6708	8.139	2	–	1
2449903.6705	8.318	2	–	1
2449904.6692	8.167	2	–	1
2449905.6591	8.210	2	–	1
2449906.6593	8.217	2	–	1
2449907.6589	8.161	2	–	1
2449908.6573	8.329	2	–	1
2450130.0134	8.094	2	1	5
2450504.8958	8.799	2	2	4
2450866.8368	8.154	1	1	3
2450934.6557	8.264	1	1	4
2450955.7222	8.144	1	1	3
2450974.6695	8.284	1	1	4
2450979.6702	8.322	1	1	4
2450986.7320	8.315	1	1	4
2451278.7070	8.104	1	2	3
2451278.7273	8.120	1	2	3
2451593.8157	8.217	2	5	5
2451706.7363	8.353	1	3	2
2451731.6859	8.195	2	5	2
2452251.0008	8.383	2	7	4
2452258.0132	8.386	2	7	4
2452348.8437	8.190	2	7	5
2452460.7124	8.324	2	7	2
2452461.6795	8.195	2	7	2
2452790.7993	8.248	1	6	5
2452807.6800	8.104	2	8	3
2452815.7371	8.288	1	6	2
2452824.7039	8.179	1	6	2
2452826.6991	8.171	1	6	2
2452828.6936	8.249	1	6	2
2453046.8944	8.013	2	9	5
2453070.8216	8.298	1	7	5
2453074.7515	7.999	2	9	3
2453139.6703	8.088	1	7	2
2453140.7700	8.379	2	9	4
2453144.6940	8.135	1	7	2
2453182.6611	8.060	1	7	2
2453184.6607	8.232	1	7	2
2453185.7171	8.155	1	7	2
2453709.0464	8.256	1	9	2
2453711.0410	8.346	1	9	2
2453711.0474	8.345	1	9	2
2453922.6616	8.243	1	9	2
2453922.6978	8.254	1	9	2
2454540.7813	8.087	1	11	3
2454807.0399	8.220	1	12	2
2454811.0305	8.260	1	12	2
2454822.0034	8.205	1	12	2
2454822.0349	8.254	1	12	2
2454999.7593	8.341	1	12	2
2455004.7444	8.298	1	12	2

Table 2. Standard Johnson V photometry of FK Com. Telescope (TEL), segments (SEG), first and last observing time (t_1 and t_n), time span and number of observations (ΔT and n)

TEL	SEG	t_1 HJD	t_n HJD	ΔT d	n
1	1	2450850.875	2450997.687	146.8	221
1	2	2451153.047	2451360.673	207.6	378
1	3	2451534.046	2451694.803	160.8	67
1	4	2451883.044	2452078.743	195.7	88
1	5	2452248.044	2452461.698	213.7	220
1	6	2452614.048	2452790.765	176.7	170
1	7	2452978.048	2453144.694	166.6	127
1	8	2453343.046	2453565.681	222.6	192
1	9	2453721.051	2453907.661	186.6	189
1	10	2454075.045	2454285.686	210.6	181
1	11	2454440.049	2454643.730	203.7	187
1	12	2454807.040	2455004.744	197.7	129
1	13	2455172.044	2455297.831	125.8	111
2	1	2450085.055	2450265.674	180.6	111
2	2	2450412.038	2450636.678	224.6	209
2	3	2450778.042	2450997.706	219.7	205
2	4	2451144.039	2451362.728	218.7	179
2	5	2451508.043	2451712.687	204.6	157
2	6	2451873.042	2452089.727	216.7	193
2	7	2452242.033	2452448.752	206.7	188
2	8	2452613.009	2452826.679	213.7	159
2	9	2452972.029	2453194.682	222.7	154

of each individual observation $V(t)$. We discard those individual $V(t)$ observations that are below $m - 2.5s$ or above $m + 2.5s$. Some observations below the $m - 2.5s$ limit may represent photometric flares (Table 1: C=3, $n = 7$). These events have been observed earlier in FK Com (Jetsu et al. 1993). All observations above the $m + 2.5s$ limit are very probably erroneous (Table 1: C=4, $n = 8$).

If two observations made during the *same* night with the *same* telescope deviate more than $0.^m06$, we discard one of them as an *outlier*. This second group of outliers contains only $n = 6$ observations (Table 1: C=5). The fraction of all *outliers*, $n = 21$, is 0.5% in all data.

All the above mentioned outliers are identified *before* our analysis. This analysis will reveal that there are many other outliers (PAPER II: Sects. 3 and 4). However, we do not reject those outliers, because they are identified only *after* the analysis.

Hackman et al. (2013) applied the Continuous Period Search method (hereafter the CPS-method) to this photometry. We refer to the model of this method as the CPS-model (Lehtinen et al. 2012, their Eq. 3). Hackman et al. (2013) modelled 1464 subsets of photometry, but they did not publish their numerical values. Their light curve periods, amplitudes, primary minimum epochs and secondary minimum epochs are now published in electronic form ¹ (Table 3).

¹ The full Table 3 is only available via anonymous ftp to cdsarc.u-strasbg.fr (130.79.128.5) or via <http://cdsarc.u-strasbg.fr/viz-bin/qcat?J/...>

Table 3. CPS-method results from [Hackman et al. \(2013\)](#). The first column gives the telescope (TEL). The remaining columns give the same subset parameters as described in the Appendix of [Lehtinen et al. \(2011\)](#): first observing time (t_1), last observing time (t_n), mean observing time (τ), statistically independent estimates (IND: 1=Yes, 0=No), number of observations (n), period ($P \pm \sigma_P$), peak to peak light curve amplitude ($A \pm \sigma_A$), epochs of primary and secondary minima ($t_{\min,1} \pm \sigma_{t_{\min,1}}, t_{\min,2} \pm \sigma_{t_{\min,2}}$). The dummy value “-1.000” denotes the cases where no estimate was obtained. The units of Heliocentric Julian Days are HJD-2 400 000. Note that we show only the ten first lines of this table. The full table is published only in electronic form. It contains 1464 lines (TEL=1: 760 lines) and (TEL=2: 704 lines).

TEL	t_1 HJD	t_n HJD	τ HJD	IND	n	P d	σ_P d	A mag	σ_A mag	$t_{\min,1}$ HJD	$\sigma_{t_{\min,1}}$ d	$t_{\min,2}$ HJD	$\sigma_{t_{\min,2}}$ d
1	50850.875	50874.887	50863.555	1	29	2.4129	0.0036	0.059	0.006	50851.594	0.032	-1.000	-1.000
1	50851.871	50875.883	50865.793	0	28	2.4154	0.0029	0.059	0.004	50854.043	0.034	-1.000	-1.000
1	50852.867	50876.883	50867.895	0	29	2.4141	0.0036	0.051	0.004	50853.980	0.031	-1.000	-1.000
1	50855.867	50878.809	50870.176	0	31	2.4196	0.0033	0.050	0.003	50856.395	0.027	-1.000	-1.000
1	50856.863	50880.867	50872.070	0	32	2.4155	0.0034	0.047	0.003	50858.812	0.029	-1.000	-1.000
1	50861.852	50885.855	50876.176	0	39	2.3930	0.0037	0.044	0.002	50863.754	0.029	-1.000	-1.000
1	50867.836	50891.840	50878.883	0	43	2.3923	0.0078	0.042	0.003	50868.613	0.042	50870.176	0.060
1	50868.828	50892.840	50880.621	0	43	2.3852	0.0051	0.041	0.003	50871.016	0.035	50870.215	0.057
1	50872.820	50896.828	50884.023	0	49	2.3699	0.0059	0.040	0.004	50875.008	0.041	50873.477	0.036
1	50873.820	50897.832	50885.551	0	49	2.3732	0.0061	0.039	0.004	50875.004	0.051	50875.844	0.037

3 MODELS

Our notation for a $V(t)$ magnitude observation made at an observing time $t = t_i$ is $y_i = y(t_i)$. The time span of these n observations is $\Delta T = t_n - t_1$. We fit a second order polynomial $h(t)$ to the y_i data of each individual segment. This polynomial is used to eliminate the seasonal changes of the mean brightness of FK Com. The analysed data are

$$y'_i = y(t_i) - h(t_i) = y_i - h_i. \quad (1)$$

We use this second order polynomial $h(t)$ in all segments, because higher orders tend to fluctuate at the ends of some segments. It would not be consistent or objective to vary the order of this polynomial in different segments. However, we will mention if this second order polynomial can, or can not, reproduce the changes of the mean brightness in individual segments (PAPER II: Sects. 3 and 4).

The abbreviation DATA_{x,y} is hereafter used for the TEL=x observations in segment SEG=y. Our notations for the mean and the standard deviation of y'_i are $m_{y'}$ and $\sigma_{y'}$. We model each segment of the y'_i data with the two and one period models.

3.1 Two period model (2P-model)

The complex 2P-model has two parts. The first part is

$$g_1(t) = g_1(t, \bar{\beta}_1) = \sum_{k=1}^{K_1} B_k \cos(k2\pi f_1 t) + C_k \sin(k2\pi f_1 t), \quad (2)$$

where $K_1 = 2$. Higher K_1 values are unnecessary, because the detection of three minima in the photometric light curve is practically impossible (e.g. [Lehtinen et al. 2011](#), their Sect. 3.2). The five free parameters are the amplitudes B_1, B_2, C_1 and C_2 , and the frequency f_1 . The frequency units are $[f] = \text{d}^{-1}$. The vector of free parameters is $\bar{\beta}_1 = [B_1, B_2, C_1, C_2, f_1]$. In every segment, we determine the following parameters of the $g_1(t)$ function

$$P_1 = \text{period} = f_1^{-1}$$

$$A_1 = \text{peak to peak amplitude}$$

$$t_{g1,\min,1} = \text{epoch of primary (i.e. deeper) minimum}$$

$$t_{g1,\min,2} = \text{epoch of secondary minimum (if present)}$$

The units are $[P_1] = \text{d}$, $[A_1] = \text{mag}$ and $[t_{g1,\min,1}] = [t_{g1,\min,2}] = \text{HJD} - 2\,400\,000$. We use the epoch of the first primary and secondary minimum within each individual segment. The phases of $g_1(t)$ are computed from

$$\phi_1 = \text{FRAC}[(t - t_0)/P_1], \quad (3)$$

where $\text{FRAC}[x]$ removes the integer part of its argument x , and $t_0 = t_1$ = the first observing time of the segment data.

The second part of the 2P-model is

$$g_2(t) = g_2(t, \bar{\beta}_2) = \sum_{k=1}^{K_2} D_k \cos(k2\pi f_2 t) + E_k \sin(k2\pi f_2 t), \quad (4)$$

where $K_2 = 2$ and $\bar{\beta}_2 = [D_1, D_2, E_1, E_2, f_2]$. The following parameters

$$P_2 = \text{period} = f_2^{-1}$$

$$A_2 = \text{peak to peak amplitude}$$

$$t_{g2,\min,1} = \text{epoch of primary minimum}$$

$$t_{g2,\min,2} = \text{epoch of secondary minimum (if present)}$$

of the $g_2(t)$ function are determined for every segment. The units are the same as those used for the $g_1(t)$ function. We compute the phases of $g_2(t)$ from

$$\phi_2 = \text{FRAC}[(t - t_0)/P_2], \quad (5)$$

where $t_0 = t_1$, as in Eq. 3.

These two parts are combined in the complex 2P-model

$$g_C(t) = g_C(t, \bar{\beta}_C) = g_1(t, \bar{\beta}_1) + g_2(t, \bar{\beta}_2). \quad (6)$$

This nonlinear model has $p_C = 10$ free parameters $\bar{\beta}_C = [\bar{\beta}_1, \bar{\beta}_2]$. Note that the functions $g_1(t)$ and $g_2(t)$ have unique phases (Eqs. 3 and 5), but no such phases exist for the $g_C(t)$ function which is constantly changing in time.

3.2 One period model (1P-model)

The simple 1P-model is

$$g_S(t) = g_S(t, \bar{\beta}_S) = \sum_{k=1}^{K_3} F_k \cos(k2\pi f_3 t) + G_k \sin(k2\pi f_3 t), \quad (7)$$

where $K_3 = 2$ and $\bar{\beta}_S = [F_1, F_2, G_1, G_2, f_3]$. There are $p_S = 5$ free parameters in this nonlinear model.

We determine the following parameters

$$\begin{aligned} P_3 &= \text{period} = f_3^{-1} \\ A_3 &= \text{peak to peak amplitude} \\ t_{S,\min,1} &= \text{epoch of primary minimum} \\ t_{S,\min,2} &= \text{epoch of secondary minimum (if present)} \end{aligned}$$

of the $g_S(t)$ function. The units are the same as those of the $g_1(t)$ and $g_2(t)$ functions. The phases of $g_S(t)$ are

$$\phi_3 = \text{FRAC}[(t - t_0)/P_3], \quad (8)$$

where $t_0 = t_1$, as in Eq. 3.

The 1P-method is a ‘‘one-dimensional’’ period finding method because it searches for only one periodicity in the data. We will consistently use the notations f_3 , P_3 and A_3 also for the frequencies, the periods and the amplitudes of all other one-dimensional period finding methods that are mentioned in this study.

3.3 Nested models

The complex model of Eq. 6 and the simple model of Eq. 7 are nested. They represent the same model if

$$\begin{aligned} \text{CASE}_1: & f_1 = f_2 \text{ in Eqs. 2 and 4} \\ \text{CASE}_2: & B_1 = B_2 = C_1 = C_2 = 0 \text{ in Eq. 2} \\ \text{CASE}_3: & D_1 = D_2 = E_1 = E_2 = 0 \text{ in Eq. 4} \end{aligned}$$

We denote the cases where the complex model approaches the simple model with

$$g_C \rightarrow g_S. \quad (9)$$

The 2P-model ‘‘breaks down’’ when this happens. The alternatives when the 2P-model and the 1P-model are the same model occur in these three cases

$$f_1 - f_2 \rightarrow 0 \quad (10)$$

$$A_1/A_2 \rightarrow 0 \quad (11)$$

$$A_2/A_1 \rightarrow 0. \quad (12)$$

The residuals of the complex model

$$\epsilon_i = y_i - g_C(t_i) \quad (13)$$

give the sum of squared residuals $R_C = \sum_{i=1}^n \epsilon_i^2$. The simple model $g_S(t)$ residuals

$$\epsilon_i = y_i - g_S(t_i) \quad (14)$$

give $R_S = \sum_{i=1}^n \epsilon_i^2$. We compute the test statistic

$$F = \left(\frac{R_S}{R_C} - 1 \right) \left(\frac{n - p_C - 1}{p_C - p_S} \right). \quad (15)$$

The null hypothesis is

H_0 : ‘‘The complex model $g_C(t)$ does not provide a significantly better fit than the simple model $g_S(t)$.’’

Under H_0 , the test statistic of Eq. 15 has an F distribution with (ν_1, ν_2) degrees of freedom, where $\nu_1 = p_C - p_S$ and $\nu_2 = n - p_C$ (Draper & Smith 1998). The probability that F reaches or exceeds a fixed level F_0 is called the critical level $Q_F = P(F \geq F_0)$. We will reject H_0 , if and only if

$$Q_F < \gamma_F = 0.001, \quad (16)$$

where γ_F is a pre-assigned significance level. It represents the probability of falsely rejecting H_0 when it is in fact true.

4 EARLIER 2P-model ANALYSIS

If the frequencies f_1 and f_2 in Eqs. 2 and 4 are unknown free parameters, the $g_C(t)$ model of Eq. 6 is nonlinear and there is no unique least squares fit solution. This $g_C(t)$ model becomes linear, if these f_1 and f_2 frequencies are fixed to some known numerical constant values, like $f_1 = 1/P_{\text{act}}$ and $f_2 = 1/P_{\text{orb}}$ in Jetsu et al. (2017). In this case, the solutions for the eight remaining free parameters of a least squares fit, the amplitudes $B_1, B_2, C_1, C_2, D_1, D_2, E_1$ and E_2 of the $g_1(t, \bar{\beta}_1)$ and $g_2(t, \bar{\beta}_2)$ functions, are unambiguous.

Jetsu et al. (2017) studied the long-term photometry of 14 CABSs with the 2P-model. They showed that the long-term MLC of all these CABSs followed the orbital period P_{orb} (Jetsu et al. 2017, Figs. 1-14: panels ‘‘b-g’’). These CABSs rotate synchronously, $P_{\text{orb}} \approx P_{\text{rot}}$. This means that the starspot distribution causing the MLC of these stars is stationary in the rotating reference frame. It was also shown that the line connecting the centres of the two binary components intersects the longitudes of this stationary part.

Jetsu et al. (2017) analysed the epochs of the primary minima $t_{\min,1}$ of the seasonal light curves of CABSs with the Kuiper method. This analysis revealed the presence of long-lived active longitudes rotating with a constant period of P_{act} . Due to the inequality $P_{\text{act}} \neq P_{\text{orb}}$, the seasonal light curve minima connected to the former period migrate in the rotating reference frame, while the minima connected to the latter period do not (Jetsu et al. 2017, Figs. 15-27: tilted non-stationary and horizontal stationary lines in panels ‘‘a’’).

Two segments of the photometry of RS CVn binary σ Gem were modelled by using $f_1 = 1/P_{\text{act}}$ and $f_2 = 1/P_{\text{orb}}$ in Eqs. 2 and 4 (Jetsu et al. 2017, Figs. 30 and 31). It was argued that *all* observed light curves of CABSs may be interference of two real light curves with periods of P_{act} (non-stationary in rotating reference frame) and $P_{\text{orb}} \approx P_{\text{rot}}$ (stationary in rotating reference frame).

Jetsu et al. (2017, Fig. 32) also modelled one segment of FK Com data with the 2P-model. They first fixed $f_1 = 1/P_{\text{act}}$ in Eq. 2. Their numerical value was $P_{\text{act}} = 2.^d401155 \pm 0.^d000092$ (Hackman et al. 2013). Then, they tested P_{rot} values which were $\pm 15\%$ at both sides of P_{act} . For each of these tested $f_2 = 1/P_{\text{rot}}$ in Eq. 4, they computed a test statistic $z_{\text{test}}(f_2)$ (Jetsu et al. 2017). For their chosen tested $f_1 = 1/P_{\text{act}}$ and $f_2 = 1/P_{\text{rot}}$ values, their test statistic z_{test} was equal to the test statistic that we will introduce later in PAPER II (Sect. 2.1: Eq. 2).

5 MEASURING SURFACE DIFFERENTIAL ROTATION (SDR)

5.1 Solar SDR

Howard (1994) discussed the uncertainties in all measurements of solar SDR. He emphasized that these measurements are averages of *many* features over latitude, and he then gave an example of the *real* SDR of *individual* features. His “sobering reminder” illustrated the solar SDR measurements of 36 708 sunspot groups made at Mount Wilson between the years 1917 and 1985 (Howard 1994, his Fig. 2). He emphasized that the latitude of any *individual* sunspot group did not predict its rotation period.

5.2 Stellar SDR

If the *individual* sunspot groups do not follow the law of solar SDR (see Eq. 22), then why should the *individual* starspots or starspot groups do so? More than ten *individual* SI-method surface temperature maps are available only for a few stars (see Strassmeier 2009, Table 2). The most extensive LC-method studies are typically based on about one hundred *individual* statistically independent light curve P_{phot} values (e.g. Jetsu et al. 1999; Lehtinen et al. 2016). Our intention is not to undermine the previous SI-method and LC-method studies, but it is fair to remind about the uncertainties in these stellar SDR measurements, if they truly rely on the “solar-stellar connection”.

6 SI-method

The compact answer to the *1st question* in PAPER II (Sect. 12) is based on results presented in the next Sects. 6.1-6.3.

6.1 SI-method parameters

In the SI-method, the aim is to determine the rotation periods of recognizable starspot distribution patterns at different latitudes. There are numerous different approaches (see Strassmeier 2009, 2011; Kochukhov 2016). For example, the rotation periods can be estimated directly from the surface images (e.g. Barnes et al. 2005; Balona & Abedigamba 2016), or simultaneous photometry can be used as an additional inversion constraint, or the latitudes of starspots in the surface images can be compared to the simultaneous light curves (e.g. Berdyugina et al. 1998; Korhonen et al. 2000; Hackman 2004; Korhonen et al. 2007; Cole et al. 2015).

The SI-method inversion represents an “ill posed problem”, because an infinite number of different solutions can fit the spectroscopic observations. Several stellar physical parameters are fixed *before* these inversions, e.g. inclination, rotation period and local spectral line profiles. This introduces additional uncertainty to the SI-method results (see Kochukhov 2016, his Sect 9.2.3.). One of the crucial fixed parameters in these inversions is the stellar rotation period P_{rot} value. It is fixed to some constant numerical value, like P_{phot} or P_{orb} .

The SI-method results for stellar SDR are usually measured by using the angular velocity difference

$$\Delta\Omega = \Omega_{\text{max}} - \Omega_{\text{min}} = \frac{2\pi}{P_{\text{min}}} - \frac{2\pi}{P_{\text{max}}} \quad (17)$$

(e.g. Barnes et al. 2005, their Table 1). For solar SDR, these values are $\Omega_{\text{max}} = \Omega_{\text{eq}} = 2\pi/P_{\text{eq}}$ and $\Omega_{\text{min}} = \Omega_{\text{pole}} = 2\pi/P_{\text{pole}}$, where $P_{\text{eq}} \approx 25^{\text{d}}$ and $P_{\text{pole}} \approx 35^{\text{d}}$ are the periods at the equator and the pole, i.e. the Sun has $P_{\text{eq}} < P_{\text{pole}}$.

6.2 SI-method general results

In this section, we discuss the *1st question* in the *general* context. Let us assume that the SI-method would be used to measure SDR from the observed difference between the periods of non-stationary starspots (P_{act}) and stationary starspots (P_{rot}). We compute the stellar surface differential coefficient (see Eqs. 22, 24 and 25) values from

$$|k| = \left| \frac{P_{\text{act}} - P_{\text{rot}}}{(P_{\text{act}} + P_{\text{rot}})/2} \right| \quad (18)$$

for the thirteen CABSs where the active longitude period P_{act} was detected in Jetsu et al. (2017, their Tables 1 and 3). The angular velocity range is

$$|\Delta\Omega| = \left| \frac{2\pi}{P_{\text{act}}} - \frac{2\pi}{P_{\text{rot}}} \right|. \quad (19)$$

The results are given in the order of increasing $|\Delta\Omega|$ in Table 4. The lower and upper limits are $|\Delta\Omega| = 0.0002 \text{ rad d}^{-1}$ (DM UMa) and $|\Delta\Omega| = 0.042 \text{ rad d}^{-1}$ (V711 Tau), respectively. Our lower limit, $|\Delta\Omega| \approx 0$, agrees with the results of the earlier SI-method studies because weak SDR has been observed in several stars. However, our $|\Delta\Omega|$ upper limit is about three times smaller than in Barnes et al. (2005, Table 1: 0.14 rad d^{-1}) and over ten times smaller than in Balona & Abedigamba (2016, Table 2: 0.47 rad d^{-1}).

Barnes et al. (2005) and Balona & Abedigamba (2016) give several $|\Delta\Omega|$ values for the *same* star. Even if the 2P-model were correct, the SI-methods are not so accurate that they would always give exactly the same $|\Delta\Omega|$, or equivalently the same P_{act} and P_{orb} , value for the starspots of the *same* star. This must have increased the scatter (i.e. the range) of these earlier published upper $|\Delta\Omega|$ limits. In addition to the previously mentioned inversion uncertainties, the identification of the *same* structure in temporally separated different images of the *same* star is not always unambiguous (see Sect 7.4.4: map-incompatibility). Finally, there are several additional reasons why our $|\Delta\Omega| = 0.042 \text{ rad d}^{-1}$ upper limit is certainly an underestimate, as will be explained later in Sects. 7.7. In this *general* context, the earlier published SI-method $|\Delta\Omega|$ estimates of SDR do not contradict the idea that the observed light curves of CABSs and CASSs could be interference of the two constant period (P_{act} and $P_{\text{orb}} \approx P_{\text{rot}}$) “real” light curves of the JHL-argument.

6.3 SI-method particular results

Here, we discuss the *1st question* in the *particular* context of the SI-method results presented by Berdyugina et al. (1998, II Peg) and Korhonen et al. (2000, FK Com).

Berdyugina et al. (1998) published nine surface images of II Peg between the years 1992 and 1997. Their orbital

Table 4. Sample of thirteen CABSs in Jetsu et al. (2017). Rotation period ($P_{\text{rot}} \approx P_{\text{orb}}$), active longitude rotation period (P_{act}), difference ($|P_{\text{rot}} - P_{\text{act}}|$), differential rotation coefficient (Eq. 18: $|k|$) and angular velocity difference (Eq. 19: $|\Delta\Omega|$). Note that the parameters are given in the order of increasing $|\Delta\Omega|$.

Star	$P_{\text{rot}} \approx P_{\text{orb}}$ d	P_{act} d	$ P_{\text{rot}} - P_{\text{act}} $ d	$ k $	$ \Delta\Omega $ rad d ⁻¹
DM UMa	7.492 ± 0.009	7.4898 ± 0.0008	0.0022 ± 0.0090	0.0003 ± 0.0012	0.0002 ± 0.0010
HK Lac	24.4284 ± 0.0005	24.40 ± 0.01	0.028 ± 0.010	0.00116 ± 0.00041	0.00030 ± 0.00011
V1149 Ori	53.57465 ± 0.00072	53.14 ± 0.06	0.435 ± 0.060	0.0081 ± 0.0011	0.00096 ± 0.00013
EL Eri	48.263 ± 0.206	47.69 ± 0.02	0.57 ± 0.21	0.0119 ± 0.0043	0.00156 ± 0.00056
BM CVn	20.6252 ± 0.0018	20.513 ± 0.006	0.1122 ± 0.0063	0.00545 ± 0.00031	0.001666 ± 0.000093
II Peg	6.724333 ± 0.000010	6.7119 ± 0.0007	0.01243 ± 0.00070	0.00185 ± 0.00010	0.001731 ± 0.000098
σ Gem	19.604471 ± 0.000022	19.497 ± 0.005	0.1075 ± 0.0050	0.00550 ± 0.00026	0.001767 ± 0.000083
HU Vir	10.387522 ± 0.000031	10.419 ± 0.001	0.0315 ± 0.0010	0.003026 ± 0.000096	0.001827 ± 0.000058
XX Tri	23.96924 ± 0.00092	23.77 ± 0.01	0.199 ± 0.010	0.00835 ± 0.00042	0.00220 ± 0.00011
V1762 Cyg	28.58973 ± 0.00002	28.17 ± 0.02	0.420 ± 0.020	0.01479 ± 0.00071	0.00327 ± 0.00016
FG UMa	21.35957 ± 0.00040	21.12 ± 0.01	0.240 ± 0.010	0.01128 ± 0.00047	0.00334 ± 0.00014
EI Eri	1.947227 ± 0.000008	1.9545 ± 0.0008	0.00727 ± 0.00080	0.00373 ± 0.00041	0.0120 ± 0.0013
V711 Tau	2.83774 ± 0.00001	2.8924 ± 0.0002	0.05466 ± 0.00020	0.019078 ± 0.000069	0.04184 ± 0.00015

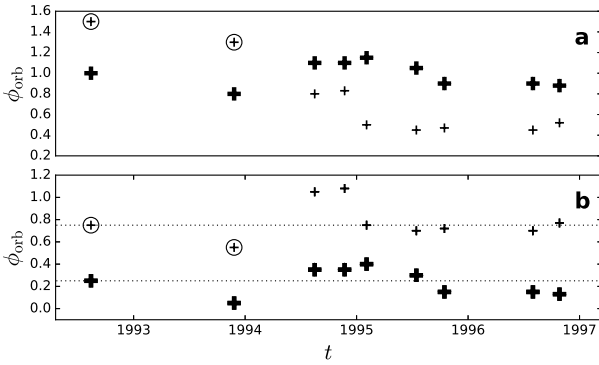


Figure 1. Orbital phases for starspots of II Peg detected with the SI-method. (a) Larger starspots (heavier crosses) and smaller starspots (lighter crosses) with the ephemeris of Eq. 20 (Berdyugina et al. 1998, their Fig. 4). The two highlighted lighter crosses are shifted one orbital round downwards in the next panel. (b) Same data with the ephemeris of Eq. 21. The horizontal dotted lines show the orbital phases $\phi_{\text{orb}} = 0.25$ and 0.75 . Otherwise as in (a).

phase ephemeris was

$$\text{HJD } 2449582.9268 + 6.724333E. \quad (20)$$

Their zero epoch was equal to that given in Jetsu et al. (2017, “Ac” epoch in their Table 2). Berdyugina et al. (1998) used the P_{orb} value of Eq. 20 in the SI-method inversions. Our Fig. 1a reproduces their phase plot for the larger and smaller starspots identified with the SI-method. Berdyugina et al. (1998) concluded that this diagram shows two active longitudes, and that a flip–flop event occurred in the year 1994.

Jetsu et al. (2017) used the orbital period ephemeris

$$\text{HJD } 2449581.246 + 6.724333E \quad (21)$$

for II Peg. Their P_{orb} was the same as in Eq. 20, but their zero epoch was $\Delta t = P_{\text{orb}}/4 \equiv \Delta\phi_{\text{orb}} = 0.25$ earlier than in Eq. 20 (Jetsu et al. 2017, “Ab” epoch in their Table 2). One of their main results was that all photometric minima of II Peg concentrated close to $\phi_{\text{orb}} = 0.25$ between the

years 1988 and 1997 (Jetsu et al. 2017, their Fig. 27a). In other words, the stationary part of the light curve ($P_{\text{orb}} = P_{\text{rot}}$) dominated during this nine year time interval which overlaps the four year time interval of the SI-method images in Berdyugina et al. (1998).

Our Fig. 1b shows the phases of the same starspots as in Fig. 1a, except that we use the ephemeris of Eq. 21. Unlike Berdyugina et al. (1998), we do not deliver evidence for a flip–flop event by adding one extra orbital round to the two first ϕ_{orb} values of smaller starspots (Figs. 1ab: two highlighted lighter crosses). The starspots of the first image in the year 1992 are exactly at $\phi_{\text{orb}} = 0.25$ and $\phi_{\text{orb}} = 0.75$, respectively. All larger starspots are at both sides of phase $\phi_{\text{orb}} = 0.25$. Most of the smaller starspots concentrate close to $\phi_{\text{orb}} = 0.75$. The simultaneous MLC of II Peg also confirms that the main activity concentrated on the longitude coinciding with the line connecting the centres of the two binary components (Jetsu et al. 2017, Fig. 14d–e: $\phi_{\text{orb}} = 0.25$). Berdyugina et al. (1998) noted that the mean latitudes of these starspots discovered with the SI-method remained approximately the same in all images. This is a convincing *particular* case, where the SI-method detects a stationary starspot of II Peg rotating with a constant period $P_{\text{orb}} = P_{\text{rot}}$ during a time interval of over four years.

Korhonen et al. (2000) published six surface images of FK Com between the years 1994 and 1997. They used the period $P_{\text{phot}} = 2.^{\text{d}}4002466 \pm 0.^{\text{d}}0000056$ in the SI-method image inversions. Comparison of their six images revealed the presence of long-lived starspots rotating with a constant period $P_{\text{SI}} = 2.^{\text{d}}4037 \pm 0.^{\text{d}}0005$. The dates of these images overlap the time interval of our photometry between the years 1995 and 1997, except for the year 1994. The thirteen first statistically independent $t_{\text{min},1}$ epochs in our Table 3 (IND=1) are between the years 1995.43 and 1997.41. The K-method analysis of these thirteen epochs gives $P_{\text{act}} = 2.^{\text{d}}4035 \pm 0.^{\text{d}}0005$. The $P_{\text{SI}} - P_{\text{act}}$ difference is only $0.^{\text{d}}0002 \pm 0.^{\text{d}}0007$. The latitude range of the starspots detected with the SI-method was between 45° and 70° , and the migration of these starspots followed “solid body rotation”(Korhonen et al. 2000). In this *particular* case, the

SI-method undoubtedly detects a long-lived non-stationary starspot of FK Com rotating with a constant period P_{act} .

The starspots detected in the above two *particular* SI-method studies by Berdyugina et al. (1998) and Korhonen et al. (2000) were long-lived and rotated with a constant angular velocity, as predicted by the JHL-argument. This type of stability is quite common in surface images. For example, the sequence 37 consecutive surface images during 57 nights show that the strongest starspot in V711 Tau appears to be nearly stationary in the rotating reference frame (Strassmeier & Bartus 2000, their Fig. 8: starspot “A”). Our answer to the *1st question* is that the *general* and the *particular* evidence strongly indicates that the P_{act} and $P_{\text{rot}} \approx P_{\text{orb}}$ periods of the JHL-argument have already been detected with the SI-method.

7 LC-method

We give compact answers to the *2nd question* and the *3rd question* in PAPER II (Sect. 12). These answers are based on the results presented in Sects. 7.3-7.4.1.

7.1 LC-method parameters

In the LC-method approach, the most widely used period finding method is the Lomb-Scargle periodogram (hereafter the LS-method, Lomb 1976; Scargle 1982). It is equivalent to finding the best least squares sinusoidal model for the data (hereafter LS-model). The LS-method is a one-dimensional period finding method because it determines only one period value for the data. There are numerous other one-dimensional period finding methods that can search for more complex models in the data (e.g. Lehtinen et al. 2011, the CPS-method).

The LC-methods usually use the following approximation for the law of solar SDR

$$P(b) = \frac{P_{\text{eq}}}{1 - k \sin^2 b}, \quad (22)$$

where b is the latitude, P_{eq} is the rotation period at the equator and k is the SDR coefficient (e.g. Hall & Busby 1990; Hall 1991, solar $k = k_{\odot} = 0.186$). A useful parameter is

$$h = \sin^2(b_{\text{max}}) - \sin^2(b_{\text{min}}), \quad (23)$$

where b_{min} and b_{max} are the minimum and maximum latitudes of starspot formation. The largest possible latitude range, $b_{\text{min}} = 0^\circ$ and $b_{\text{max}} = \pm 90^\circ$, gives $h = 1$. All other latitude ranges give $h < 1$. This leads to the relation

$$k = \frac{\Delta P}{h P_{\text{eq}}}, \quad (24)$$

where $\Delta P = |P(b_{\text{max}}) - P(b_{\text{min}})| = P_{\text{phot,max}} - P_{\text{phot,min}}$ is the difference between the largest and smallest observed photometric rotation period P_{phot} in any particular star. Since $h \leq 1$, the LC-methods use the lower limit

$$|k| \geq \frac{P_{\text{phot,max}} - P_{\text{phot,min}}}{P_{\text{phot,mean}}} \quad (25)$$

for the absolute value of stellar SDR coefficient, where $P_{\text{phot,mean}}$ is the mean of all observed values of P_{phot} . There are four uncertainties in this relation. Firstly, $P_{\text{phot,mean}} \approx (P_{\text{phot,max}} + P_{\text{phot,min}})/2$ must be used as an approximate

estimate for P_{eq} of Eq. 24, because it is not known whether $P_{\text{phot,min}}$ or $P_{\text{phot,max}}$ represents P_{eq} . Some LC-methods use $P_{\text{eq}} = P_{\text{phot,max}}$ (e.g. Reinhold et al. 2013). Secondly, the sign of k is unknown, where $k > 0$ represents solar and $k < 0$ represents anti-solar SDR. Thirdly, the latitude range of starspot formation, the value of h in Eqs. 23 and 24, is unknown. Fourthly, it is not known if the full range of period changes has already been observed, or does the observed $P_{\text{phot,max}} - P_{\text{phot,min}}$ difference represent an underestimate of the real range.

Another approach for measuring the range of changes for n photometric rotation periods $P_{\text{phot},i}$ (e.g. Lehtinen et al. 2016) is to use the weighted mean

$$P_w = \frac{\sum_{i=1}^n w_i P_{\text{phot},i}}{\sum_{i=1}^n w_i} \quad (26)$$

and the weighted standard deviation

$$\Delta P_w = \sqrt{\frac{\sum_{i=1}^n w_i (P_{\text{phot},i} - P_w)^2}{\sum_{i=1}^n w_i}}, \quad (27)$$

where $\sigma_{P_{\text{phot},i}}$ is the error of $P_{\text{phot},i}$ and the weights are $w_i = \sigma_{P_{\text{phot},i}}^{-2}$. Equal weights $w_i = 1$ give $P_w = m_P$ and $\Delta P_w = \sigma_P$, where m_P and σ_P are the mean and standard deviation of all observed $P_{\text{phot},i}$ values. In this case, the “three sigma” upper limit for the $P_{\text{phot},i}$ changes is

$$Z = \frac{6\Delta P_w}{P_w} = \frac{6\sigma_P}{m_P}. \quad (28)$$

The relation

$$|k| \approx Z/h \quad (29)$$

is valid, if $P_{\text{phot,max}} - P_{\text{phot,min}} \approx 6\Delta P_w$ (Jetsu et al. 2000).

7.2 LC-method results

The idea that the value of P_{phot} is connected to the stellar rotation period P_{rot} is logical. In the SDR context, the observed value of P_{phot} could tell something about the latitude of the spot. If the *observed* P_{phot} has changed, it is logical to assume that the latitude of the spot has changed. Thus, the range of P_{phot} changes could measure SDR.

Hall (1991) applied the LC-method to the photometry of 277 late-type stars. He concluded that the stellar SDR correlates strongly with $P_{\text{phot}} \approx P_{\text{rot}}$. It decreases when P_{phot} decreases. He showed that SDR was so weak in some rapidly rotating stars that it approached solid-body rotation. This general relation between P_{phot} and SDR has been amply confirmed by subsequent LC-method studies of much larger samples (e.g. Reinhold et al. 2013, 24 124 stars). We have also formulated our own LC-methods, and used them to measure stellar SDR (e.g. Jetsu & Pelt 1999; Jetsu et al. 1999; Lehtinen et al. 2011, 2016, the TSPA-method and the CPS-method). Considering all these findings, our JHL-argument runs into its next problem: what is the answer to the *2nd question*. Note that we have very good reasons for emphasizing the words *many*, *different*, *observed* and *same* in this particular question, as will become evident in the next Sects. 7.3-7.4.1.

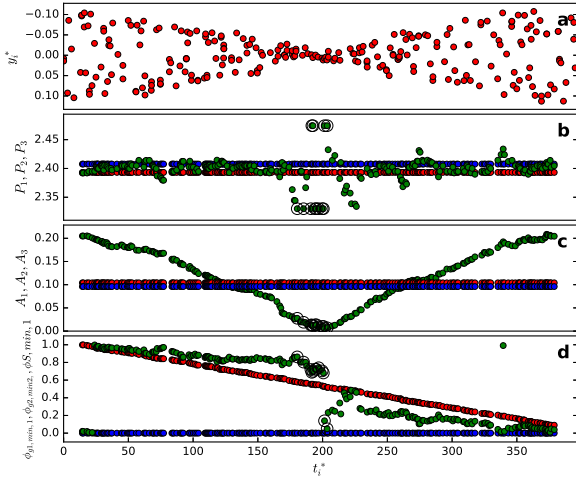


Figure 2. (a) Simulated y_i^* data of Eq. 33 for equal amplitudes $a_1 = a_2 = 0.^m05$ in Eqs. 30 and 31. (b) Periods $P_1 = 2.^d39313$ and $P_2 = 2.^d40762$ of the 2P-model are denoted with red and blue circles. The green circles show the periods P_3 detected with the LS-method. The large black circles around some green circles highlight the cases, where the highest z_{LS} periodogram value is in the beginning or in the end of the tested period interval. (c) Amplitudes $A_1 = 2a_1$ and $A_2 = 2a_2$ of the 2P-model are denoted with red and blue circles. Note that these red and blue symbols are slightly shifted apart, because they would otherwise overlap. The green circles show the peak to peak amplitudes A_3 of the LS-model sinusoids. The same models as in "b" are highlighted again. (d) The red and blue circles show the light curve minimum phases of $g_1(t) = s_1(t)$ and $g_2(t) = s_2(t)$ with P_2 in Eq. 3. The green circles show the light curve minima of the LS-method sinusoids. The highlighted models are the same as in "bc".

7.3 Simulated 2P-model data

Here, we assume that the 2P-model is correct and we simulate artificial photometric data of two different cases. The model used in creating the simulated data is the sum of two sinusoidal light curves

$$s_1(t) = a_1 \sin(2\pi f_1 t) \quad (30)$$

$$s_2(t) = a_2 \sin(2\pi f_2 t). \quad (31)$$

This model has $s_1(t) = g_1(t)$ in Eq. 2, $s_2(t) = g_2(t)$ in Eq. 4 and $s(t) = s_1(t) + s_2(t) = g_C(t)$ in Eq. 6. The peak to peak amplitudes are $A_1 = 2a_1$ and $A_2 = 2a_2$. The frequencies are fixed to $f_1 = P_1^{-1}$ and $f_2 = P_2^{-1}$, where the periods are $P_1 = 2.^d39313$ and $P_2 = 2.^d40762$. These period values are taken from the ephemerides of Eqs. 20 and 21 of PAPER II. We compute the lap cycle period

$$P_{\text{lap}} = |P_1^{-1} - P_2^{-1}|^{-1} = |f_1 - f_2|^{-1} \approx 398^d \quad (32)$$

of these periodicities (Jetsu et al. 2017, their Eq. 4). The interference pattern of $s(t) = s_1(t) + s_2(t)$ is repeated regularly after every $\Delta T = P_{\text{lap}}$. Hence, the time span of the simulated data segment is fixed to $\Delta T = P_{\text{lap}}$. We use multiples of sidereal day $P_{\text{sid}} = 0.^d99726958$ to create $n^* = 250$ time points

$$t_i^* = i^* P_{\text{sid}} + \delta t_i^*,$$

where i^* are a random sample of integers $1 \leq i^* \leq 398$. Any particular integer i^* value is used as many times as the

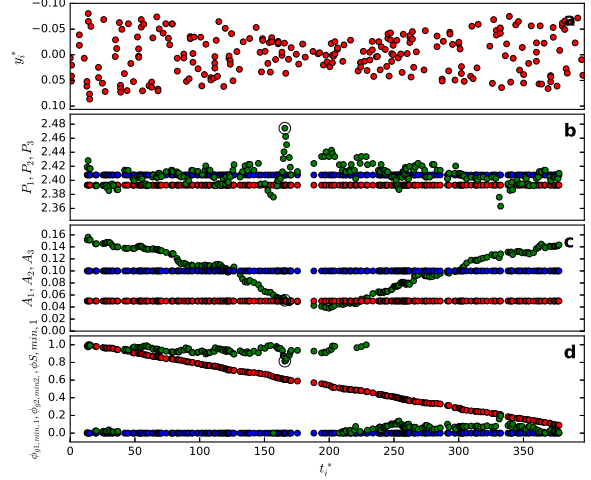


Figure 3. Simulated y_i^* data of Eq. 33 for unequal amplitudes $a_1 = 0.^m025$ in Eq. 30 and $a_2 = 0.^m050$ in 31, otherwise as in Fig. 2.

random selection favours it. The simulated random shifts δt_i^* at both sides of the mid-nights $i^* P_{\text{sid}}$ are evenly distributed between $-0.^d2$ and $0.^d2$. The simulated data are

$$y_i^* = s(t_i^*) + \epsilon_i^*, \quad (33)$$

where ϵ_i^* are a random sample of $n^* = 250$ residuals drawn from a Gaussian distribution with a zero mean and a standard deviation of $0.^m008$.

Inside the simulated segment, we select datasets containing all y_i^* that are within a sliding window of $\Delta T = 30^d$. We apply the LS-method to all those datasets that contain at least $n = 12$ values of y_i^* . Similar sliding window one-dimensional period analysis has been applied to real photometry, e.g. by Distefano et al. (2016, the LS-method) or Lehtinen et al. (2016, the CPS-method). The maximum and minimum values of tested $f_3 = P_3^{-1}$ frequencies of the LS-model are

$$f_{\text{min}} = (1 - a)f_{\text{mid}}, \quad f_{\text{max}} = (1 + a)f_{\text{mid}}, \quad (34)$$

where $P_{\text{mid}} = (P_1 + P_2)/2$, $f_{\text{mid}} = P_{\text{mid}}^{-1}$, and $a = 0.03$. This is the $\pm 3\%$ range at both sides of f_{mid} .

7.3.1 $a_1 = a_2$ simulation (TEST $_{a_1=a_2}$)

In the first case, we use equal amplitudes $a_1 = a_2 = 0.^m05$ in Eqs. 30 and 31. We will hereafter refer to these simulations as TEST $_{a_1=a_2}$. The results are shown in Fig. 2.

The amplitude of the simulated data decreases to zero during the first half of the segment and then increases back to its original level during the last half (Fig. 2a). This pattern is repeated during every lap cycle $\Delta T = P_{\text{lap}}$ (Eq. 32), because the interference of these two sinusoids is regular. The periods P_1 and P_2 of the simulated model do not change (Fig. 2b: red and blue circles). However, the periods detected with the LS-method show large variation (Fig. 2b: green circles), especially when the amplitude of the simulated data approaches zero in the middle of the segment. There are cases where the highest LS-method periodogram z_{LS} value is at the end of the tested period interval (Fig. 2b: highlighted green circles). This is a clear sign of that the tested

period interval is too narrow for this particular period finding method. The amplitudes A_1 and A_2 of the 2P-model remain unchanged (Fig. 2c: red and blue circles). The peak to peak amplitudes A_3 of the sinusoidal LS-models vary between $0.^m0$ and $0.^m2$ (Fig. 2c: green circles). The phases of the light curve minima of $s_2(t)$ are stable with P_2 in Eq. 3 (Fig. 2d: blue circles), while those of $s_1(t)$ show regular linear migration (Fig. 2d: red circles). Finally, the minima of the sinusoidal models detected with the LS-method show minor linear changes and an abrupt 0.5 phase shift in the middle of the segment (Fig. 2d: green circles). This phase shift occurs when the amplitude A_3 approaches zero, and this event coincides with the cases when no periodicity is detected with the LS-method (Figs. 2bcd: highlighted green circles). We emphasize that this half a rotation phase shift occurs in *every* simulated artificial data sample of Eq. 33 when $a_1 = a_2$.

7.3.2 $a_1 < a_2$ simulation ($\text{TEST}_{a_1 < a_2}$)

In the second case, the amplitudes are unequal: $a_1 = 0.^m025$ in Eq. 30 and $a_2 = 0.^m05$ in Eq. 31. These simulations are hereafter referred to as $\text{TEST}_{a_1 < a_2}$.

The amplitude of the simulated data first decreases from $0.^m15$ to $0.^m05$, and then increases back to $0.^m15$ (Fig. 3a). The periods P_1 and P_2 do not, of course, change (Fig. 3b: red and blue circles). There is large variation in the P_3 periods detected with the LS-method (Fig. 3b: green circles). This variation is largest in the middle of the segment when the amplitude is lowest. The amplitudes A_1 and A_2 of the 2P-model do not change (Fig. 3c: red and blue circles). The peak to peak amplitudes A_3 of the LS-models vary regularly between $0.^m05$ and $0.^m15$ (Fig. 3c: green circles). The same phases of the light curve minima of $s_1(t)$ and $s_2(t)$ as in the previous Fig. 2d are shown again in Fig. 3d (red and blue circles). The phases of the minima of the sinusoidal LS-models fluctuate (Fig. 3d: green circles). The cases when the LS-method detects no periodicity do not occur as often as in $\text{TEST}_{a_1 = a_2}$, because the amplitude does not decrease to zero in the middle of the segment (Figs. 3bcd: one highlighted circle).

7.4 Incompatibility

The $\text{TEST}_{a_1 = a_2}$ and $\text{TEST}_{a_1 < a_2}$ simulations reveal something that we will hereafter refer to as “incompatibility”. If the JHL-argument is true, this incompatibility manifests itself in the *observed* light curve periods, amplitudes and minima determined with any one-dimensional period finding method, like e.g. the LS-method or the CPS-method.

The amplitudes A_1 and A_2 of the simulated light curves are constant in the above mentioned $\text{TEST}_{a_1 = a_2}$ and the $\text{TEST}_{a_1 < a_2}$ simulations. All incompatibility effects described in the next Sects. 7.4.1-7.4.4 are even stronger in the real data, because these A_1 and A_2 amplitudes are changing. These effects are nicely illustrated in the periodogram of all data which resembles a patchwork quilt (see PAPER II: Fig. A70 discussed in Sect. 9).

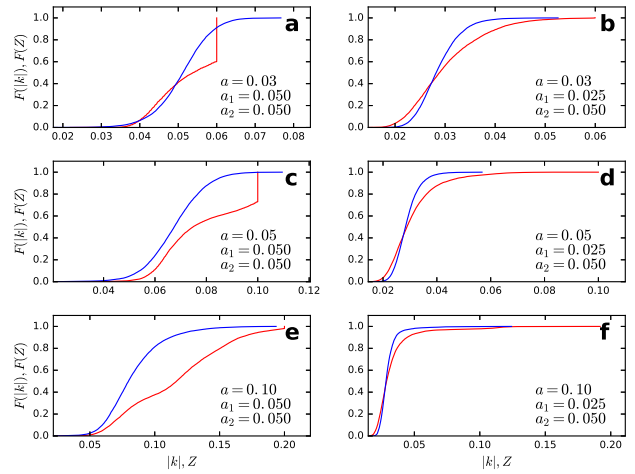


Figure 4. (a) Cumulative distribution functions $F(|k|)$ (red) and $F(Z)$ (blue) in 10 000 simulations of $\text{TEST}_{a_1 = a_2}$ with $a = 0.03$ in Eq. 34 (b) same as in “a” for $\text{TEST}_{a_1 < a_2}$. (c) $a = 0.05$ in Eq. 34, otherwise as in “a”. (d) $a = 0.05$ in Eq. 34, otherwise as in “b”. (e) $a = 0.10$ in Eq. 34, otherwise as in “a”. (f) $a = 0.10$ in Eq. 34, otherwise as in “b”.

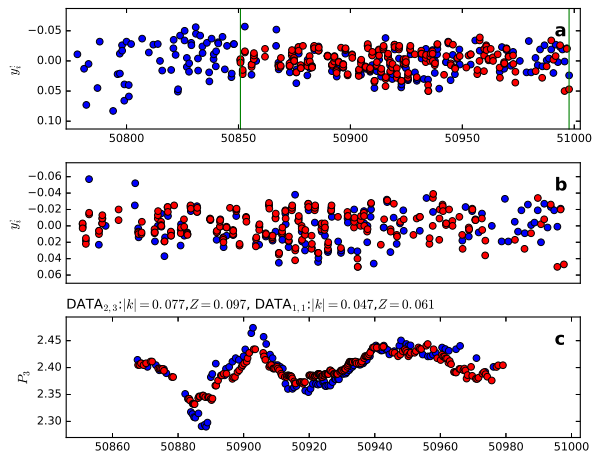


Figure 5. (a) Overlapping $\text{DATA}_{2,3}$ and $\text{DATA}_{1,1}$ photometry (red and blue filled circles). Vertical green lines show the beginning and the end of fully overlapping observations. (b) Fully overlapping photometry. (c) Red and blue filled circles denote P_3 periods detected from the fully overlapping photometry with the LS-method. The $|k|$ and Z results are given above this panel.

7.4.1 Period-incompatibility

The $\text{TEST}_{a_1 = a_2}$ and $\text{TEST}_{a_1 < a_2}$ simulations both show that the LS-method detects spurious P_3 periods and spurious P_3 changes although the 2P-model periods P_1 and P_2 do not change.

The P_3 period results in Fig. 2b represent only one particular simulated $\text{TEST}_{a_1 = a_2}$ case where $a = 0.03$ in Eq. 34, and $a_1 = a_2 = 0.050$ in Eqs. 30 and 31. We simulated 10 000 such cases having this same a , a_1 and a_2 combination. Each case gave us one estimate of $|k|$ (Eq. 25) and Z (Eq. 28). The cumulative distribution functions $F(|k|)$ and

$F(Z)$ of these parameters are shown in Fig. 4a (red and blue continuous lines). The parameter ranges are approximately $0.035 \leq |k| \leq 0.06$ and $0.03 \leq Z \leq 0.07$. A steep rise of $F(|k|)$ occurs at $2a = 0.06$. The probability for $F(|k| \geq 2a)$ is nearly 0.5. The $|k|$ values can not exceed this $2a$ limit, because the maxima and the minima of detected P_3 values have to be within the tested period interval (Eq. 34). In nearly half of the 10 000 cases, the LS-method detects P_3 periods over the whole tested period interval $(1 \pm a)P_{\text{mid}}$. The shape of $F(Z)$ resembles that of a Gaussian cumulative distribution function.

The results for 10 000 simulated $\text{TEST}_{a_1 < a_2}$ cases with $a = 0.03$, $a_1 = 0.025$ and $a_2 = 0.050$ are shown in Fig. 4b. The approximate ranges are $0.02 \leq |k| \leq 0.06$ and $0.02 \leq Z \leq 0.05$. The minimum peak to peak amplitude of the simulated $s(t)$ light curve is $A_3 = 2a_1 = 0.050$ in these $\text{TEST}_{a_1 < a_2}$ simulations. Since A_3 does not decrease to zero, as in $\text{TEST}_{a_1 = a_2}$, the LS-method succeeds in detecting periodicities that are within the tested period interval.

The combination $a = 0.05$, $a_1 = 0.050$ and $a_2 = 0.050$ (Fig. 4c) shows what happens in $\text{TEST}_{a_1 = a_2}$ with a longer tested $\pm 5\%$ period interval. The $|k|$ and Z ranges increase, and the “expected” steep $F(|k|)$ rise occurs at $2a = 0.10$. The $\text{TEST}_{a_1 < a_2}$ combination $a = 0.05$, $a_1 = 0.025$ and $a_2 = 0.050$ shows no steep $F(|k|)$ rise at $|k| = 2a$ (Fig. 4d). The results for $a = 0.10 \equiv \pm 10\%$ are shown in Figs. 4ef. The LS-method keeps on finding P_3 periods over the whole period interval in $\text{TEST}_{a_1 = a_2}$ simulations, because the $|k|$ maximum is at $2a = 0.20$. The general result is that the $|k|$ and Z ranges increase when the tested range, a in Eq. 34, increases.

The simulations shown in Figs. 4a–f also reveal that the relation $|k| \approx Z/h$ of Eq. 29 is a poor approximation. This is no surprise, because $|k|$ is computed from *two* individual P_3 values, while Z is computed from *all* P_3 values.

If the JHL-argument is correct, our simulations also predict that two observers *observing* the light curve of *same* star during the *same* time interval will get *different* P_3 , $|k|$ and Z values with the LS-method. We show the temporally overlapping DATA_{2,3} and DATA_{1,1} photometry in Fig. 5a. The fully overlapping data are shown in Fig. 5b. We divide these fully overlapping data into subsets using a sliding window of 30 days, and analyse all subsets having at least 12 observations with the LS-method (Eq. 34: $a = 0.05$). In Fig. 5c, we show the P_3 , $|k|$ and Z results for the fully overlapping data of segments DATA_{2,3} and DATA_{1,1}. The respective results for all temporally overlapping pairs of segments are given in Table 5. These results confirm the above prediction.

If the JHL-argument is true, no-one ever gets the same LS-method analysis results from the simultaneous photometry of the same star. This general result applies to all one-dimensional period finding methods. All the above findings are amazing considering that the underlying 2P-model, $g_C(t) = s(t) = s_1(t) + s_2(t)$, does not change at all. Since this period incompatibility solves the *2nd question*, it is easy to the answer the *3rd question* (see PAPER II: Sect. 12).

7.4.2 Amplitude-incompatibility

The *observed* light curve amplitudes A_3 in Figs. 2c and 3c do not certainly tell anything about the *real* light curve amplitudes A_1 and A_2 of the 2P-model. We will hereafter refer to

Table 5. $|k|$ and Z for fully overlapping real observations. Columns 1 and 4 give the temporally overlapping segments. The other columns give the $|k|$ and Z values for fully overlapping data.

	$ k $	Z		$ k $	Z
DATA _{2,3} :	0.077	0.097	DATA _{1,1} :	0.047	0.061
DATA _{2,4} :	0.100	0.141	DATA _{1,2} :	0.063	0.085
DATA _{2,5} :	0.022	0.032	DATA _{1,3} :	0.012	0.016
DATA _{2,6} :	0.014	0.018	DATA _{1,4} :	0.010	0.012
DATA _{2,7} :	0.079	0.068	DATA _{1,5} :	0.070	0.096
DATA _{2,8} :	0.051	0.062	DATA _{1,6} :	0.025	0.032
DATA _{2,9} :	0.088	0.091	DATA _{1,7} :	0.048	0.038

this problem as “amplitude-incompatibility”. It is common for all one-dimensional period finding methods.

The period analysis of the observed amplitudes A_3 can sometimes be used to determine the numerical value for the lap cycle period P_{lap} of Eq. 32. These P_{lap} cycles were clearly present in the observed A_3 amplitudes of thirteen CABSs (Jetsu et al. 2017, their Figs. 15–27). The numerical P_{lap} value can also be used to indirectly estimate other 2P-model parameters (see Sect. 7.7).

7.4.3 Minima-incompatibility

The one-dimensional period finding methods also suffer from something that we will hereafter refer to as “minima-incompatibility”. If we would analyse the light curve minima epochs of Figs. 2d and 3d with the K-method, we would not detect the P_1 period or the P_2 period. We could detect P_2 when $A_1 = 0$ (CASE₂) or P_1 when $A_2 = 0$ (CASE₃). Unfortunately, the observed light curve does not give us any unambiguous information of when $A_1 = 0$ or when $A_2 = 0$. Thus, the next logical step is to begin to search for the answers to the *4th question*, the *5th question* and the *6th question*.

7.4.4 Map-incompatibility

If the JHL-argument is true, the non-stationary and stationary starspots migrate with different Ω angular velocities. In this case, the comparison of surface images from different years can lead to false identifications of the non-stationary (P_{act}) and the stationary (P_{orb} or P_{rot}) starspots. In general, there is no unique period in the $g_C(t)$ model for comparing the longitudinal difference between two starspots, say A and B, over a longer period of time. It is also uncertain, if A moves forwards or backwards with respect to B. The 2P-model predicts that one can reliably compare two surface images of the *same* star with the *same* constant period only if the time difference of these surface images is much shorter than $P_{\text{lap}}/2$. For example, the lap cycle period of FK Com is only $P_{\text{lap}} = 398^{\text{d}}$. This is comparable to the typical one year gap between observing seasons. We will hereafter refer to this problem as “map-incompatibility”. This effect resembles the shuffling of cards. The current order of cards (i.e. longitudes of starspots A and B) does not give any information about the order before the shuffling. This effect has certainly been overlooked or underestimated in earlier SI-method studies, like Washuettl et al. (2009, EI Eri: eleven years), Lindborg et al. (2011, II Peg: six years)

or Hackman et al. (2013, FK Com: 13 years). This map incompatibility must have caused numerous misidentifications of the rotating structures, because there are no unique phases or longitudes in the constantly changing 2P-model. Such misidentifications have increased the range of $|\Delta\Omega|$ estimates, e.g. in Barnes et al. (2005) or Balona & Abedigamba (2016), which were discussed earlier in Sect 6.

7.5 Dead end

Jetsu et al. (2017) assumed that the K-method analysis of the $t_{\min,1}$ minima epochs of Table 3 would give an unambiguous P_{act} value for FK Com (the 4th question). The next step in their reasoning was to use this P_{act} value in solving an unambiguous P_{rot} value for FK Com. However, we have just shown that if the $t_{\min,1}$ minima epochs are determined with any one-dimensional period analysis method, then the minima-incompatibility prevents a unique P_{act} solution. Any particular $t_{\min,1}$ value in our Table 3 may, or may not, be connected to P_{act} and/or P_{rot} (see Sect. 7.7: MIGRATION₁, MIGRATION₂ and MIGRATION₃ alternatives). This problem could be at least partly solved, if we knew the time intervals when the interference caused by the other periodicity is absent, and only the P_{act} or P_{rot} period totally dominates the light curves of FK Com (CASE₂ or CASE₃). However, we have no way of knowing when takes place.

We could try to use the known orbital period $P_{\text{orb}} \approx P_{\text{rot}}$ to solve P_{act} , if FK Com were a binary, like the 14 CABSS studied in Jetsu et al. (2017). This *certainly known* P_{rot} could then be used to solve P_{act} in a similar way, as P_{rot} was solved by using the *presumably known* P_{act} (Jetsu et al. 2017, their Fig. 32). Unfortunately, we do not have the “luxury” of knowing the P_{rot} period of FK Com *before* the analysis.

If the JHL-argument is true, we must conclude that all our earlier one-dimensional period analyses have given spurious results, because these results suffer from incompatibility. The same applies to all one-dimensional period finding analyses of starspots done by others during the past 70 years since Kron (1947) published his first observations of starspots. Due to this incompatibility, neither one of the two P_{act} and P_{rot} periods of FK Com can be fixed before the analysis. These two periods must be solved simultaneously. At this point, we have a serious problem, because our current study of FK Com photometry has arrived at a dead end: we can not use the $t_{\min,1}$ minima epochs of Table 3 to get an unambiguous solution for the numerical P_{rot} or P_{act} period values of FK Com (the 4th question and the 5th question).

7.6 Sum of two different frequency sinusoids

In Sect. 7.3, we assumed that the 2P-model is correct and simulated artificial data with this model. Here, we show *how* these results could have been anticipated mathematically, and especially the incompatibility. The mathematical relations presented in this section explain all graphical results presented earlier in Figs. 2 and 3.

If $f_1 \approx f_2$, the solution for the sum $s(t)$ of sinusoidal light curves $s_1(t)$ and $s_2(t)$ of Eqs. 30 and 31 depends *only*

on the amplitudes a_1 and a_2 . The solutions are different for

$$a_1 = a_2 \quad (35)$$

$$a_1 \neq a_2. \quad (36)$$

If Eq. 35 is true, then

$$s(t) = s_1(t) + s_2(t) = a_a(t) \sin(2\pi f_a t), \quad (37)$$

where the amplitude is

$$a_a(t) = a_1 \sqrt{2 + 2 \cos[2\pi(f_1 - f_2)t]} \quad (38)$$

and the frequency is

$$f_a = (f_1 + f_2)/2. \quad (39)$$

This frequency of the sum $s(t)$ remains constant $f = f_a$. Hence, the P_3 periods detected with the LS-method concentrate between P_1 and P_2 in Fig. 2b. The amplitude $a_a(t)$ of Eq. 38 varies between $a_{a,\min} = 0$ and $a_{a,\max} = 2a_1$ with the lap cycle period P_{lap} . This regularity is seen in Fig. 2c. Finally, an abrupt $f_a/2$ phase shift of $s(t)$ occurs when $a_a(t)$ goes to zero, as seen in Fig. 2d.

If Eq. 36 is true, we assume that $a_1 < a_2$. In this case, the sum is

$$s(t) = s_1(t) + s_2(t) = a_b(t) \sin[2\pi f_2 t + \phi_b(t)], \quad (40)$$

where the amplitude is

$$a_b(t) = \sqrt{a_1^2 + a_2^2 + 2a_1 a_2 \cos[2\pi(f_1 - f_2)t]} \quad (41)$$

and the phase shift is

$$\phi_b(t) = \arctan \left[\frac{a_1 \sin[2\pi(f_1 - f_2)t]}{a_1 \cos[2\pi(f_1 - f_2)t] + a_2} \right]. \quad (42)$$

The $[\phi_b(t)]$ units are radians.

The amplitude $a_b(t)$ of Eq. 41 varies regularly between

$$a_{b,\min} = a_2 - a_1 \quad (43)$$

and

$$a_{b,\max} = a_1 + a_2 \quad (44)$$

during the lap cycle period P_{lap} , as seen in Fig. 3c.

The phase modulation $\phi_b(t)$ induces frequency changes of $s(t)$ between

$$f_{b,\max} = f_2 + \frac{a_1(f_1 - f_2)}{a_2 + a_1} \quad (45)$$

at the $a_{b,\max}$ epochs, and

$$f_{b,\min} = f_2 - \frac{a_1(f_1 - f_2)}{a_2 + a_1} \quad (46)$$

at the $a_{b,\min}$ epochs. These frequency changes of $s(t)$ at both sides of f_2 are repeated regularly during P_{lap} . The frequency f_2 of the stronger $s_2(t)$ sinusoid ($a_1 < a_2$) dominates these frequency changes of $s(t)$. The P_3 changes in Fig. 3b concentrate on the level of the stronger P_2 periodicity.

The maximum $\phi_b(t)$ phase shift is

$$\phi_{b,\max} = \arcsin(a_1/a_2) \quad (47)$$

to both directions. The $[\phi_{b,\max}]$ units are radians. For $a_1 = a_2$, the maximum phase shift $\phi_{b,\max}$ is $\pi/2$ radians, or equivalently $(\pi/2)/(2\pi) = 1/4$ in dimensionless phase units with f_2 . Since this shift at $a_{b,\min}$ occurs to both directions, its full range is

$$\Delta\phi_b = [\arcsin(a_1/a_2)]/\pi \quad (48)$$

in dimensionless phase units. This gives $\Delta\phi_b = 0.5$ when $a_1 = a_2$. No phase shift can exceed this limit. This abrupt phase shift occurs also when $a_1 \neq a_2$, but it is smaller. For example, the $a_1 = 0.^m048$ and $a_2 = 0.^m050$ combination causes an abrupt $\Delta\phi_b = 0.41$ phase shift at $a_{b,\min}$. The predicted phase shift in Fig. 3d is only $\Delta\phi_b = 0.17$.

In conclusion, the *observed* amplitude, period and minimum of the sum $s(t)$ fluctuate regularly with the lap period cycle P_{lap} when the condition of Eq. 36 is true.

7.7 Indirect approach

Now that we know all these different mathematical relations for the sum $s(t) = s_1(t) + s_2(t)$ presented in the previous Sect. 7.6, it is still next to impossible to figure out what happens in some particular sample of photometry. These mathematical relations do, however, give us some hope in resolving the P_{act} and P_{rot} dilemma of FK Com, because they open up several indirect approaches. Here, indirect means that we do not solve the P_1 and P_2 periods simultaneously and directly. These indirect approaches are valid only if the real light curves $g_1(t)$ and $g_2(t)$ are sinusoids (Eqs. 30 and 31). For example, the relations of Eqs. 37 and 40 show that the shape of the sum curve $s(t)$ is sinusoidal with only one minimum and maximum. If this observed $s(t)$ light curve has two minima, the indirect approaches presented below are no longer valid because at least one of the real light curves $g_1(t)$ and $g_2(t)$ can not be a sinusoid.

It has already been mentioned in Sect. 7.4.2 that the period analysis of the observed light curve amplitudes A_3 may reveal the lap cycle period P_{lap} . The relation of Eq. 32 is easier to manipulate in the frequency domain, $f_{\text{lap}} = |f_1 - f_2| = \pm(f_1 - f_2)$. This gives

$$f_1 = \pm f_1 = f_{\text{lap}} \pm f_2 \quad (49)$$

We can use the equality $f_1 = \pm f_1$, because a negative f_1 value makes no sense in this particular context. Assuming that $f_2 = P_{\text{orb}}^{-1} \approx P_{\text{rot}}^{-1}$ in CABSSs, the above relation gives two solutions for $f_1 = P_{\text{act}}^{-1}$ when $P_{\text{lap}} = f_{\text{lap}}^{-1}$ is known. If the signal of the P_{orb} period does not dominate the light curves, the migration of the light curve minimum epochs is tilted as a function of phase ϕ_2 with $P_2 = P_{\text{orb}} = f_2^{-1}$ (Eq. 5). During these time intervals, the forwards or backwards migration of these minima reveals if $P_{\text{act}}^{-1} = f_1 = f_{\text{lap}} + f_2$ or $P_{\text{act}}^{-1} = f_1 = f_{\text{lap}} - f_2$. Unfortunately, this relation of Eq. 49 does not help with any CASS, like FK Com.

There are three migration alternatives for the observed $s(t) = s_1(t) + s_2(t)$ light curve minima

MIGRATION₁: If $a_1 \approx a_2$ (Eqs. 30 and 31), the migration is linear with $(f_1 + f_2)/2$ (Eq. 39)

MIGRATION₂: If $a_1 < a_2$ (Eqs. 30 and 31), the migration is linear with f_2 and fluctuating (Eqs. 45 and 46)

MIGRATION₃: If $a_1 > a_2$ (Eqs. 30 and 31), the migration is linear with f_1 and fluctuating (Eqs. 45 and 46)

It is not easy to unambiguously separate these three alternatives from each other in the real photometric observations. Nevertheless, we know at least that the stronger signal usually dominates the linear fluctuating migration (Eqs. 45-46), because it is reasonable to assume that the cases $a_1 \approx a_2$ occur less frequently than the cases $a_1 < a_2$ or $a_1 > a_2$. When the observed $s(t)$ light curve minima $t_{\text{min},1}$ are analysed, e.g.

with the K-method, the result can be f_1 , f_2 or $(f_1 + f_2)/2$, or none of these. Different migration alternatives of CABSSs were displayed in Jetsu et al. (2017, Figs. 15-27: tilted non-stationary and horizontal stationary lines in panels “a”). We know now that there are at least three different migration alternatives even in the most simple case of two interacting sinusoids $s_1(t)$ and $s_2(t)$. For example, the minima of II Peg first concentrated close to $\phi_{\text{orb}} = 0.25$ between the years 1988 and 1997, and then these minima began to wander regularly away from this phase (Jetsu et al. 2017, their Fig. 27a). All available $t_{\text{min},1}$ light curve minima were used to determine the P_{act} value of this CABS. However, we know now that the result for P_{act} was not correct, because some $t_{\text{min},1}$ values, like those between the years 1988 and 1997, were certainly connected P_{orb} , but not to $P_{\text{act}} \neq P_{\text{orb}}$. For any particular star, the K-method may detect f_1 , f_2 or $(f_1 + f_2)/2$ depending on which one of the MIGRATION₁, MIGRATION₂ or MIGRATION₃ modes dominates. The long-term photometry of any CABS or CASS is a mixture of all these three migration alternatives, because the amplitudes $A_1 = 2a_1$ and $A_2 = 2a_2$ can change.

It may be possible to identify the time intervals when one of the above mentioned three migration modes dominates. For example, it is usually easy to notice the *particular* time intervals when P_{orb} dominates the $s(t)$ light curve minima of some CABS (Jetsu et al. 2017, e.g. II Peg). It may be possible to solve P_{act} by analysing the $t_{\text{min},1}$ values of the *other* remaining time intervals with the K-method. Finally, the observing seasons displaying a flip-flop event represent the MIGRATION₁ case having an exceptional amplitude and periodicity combination. The detection of the P_{orb} or P_{act} periods is impossible during these observing seasons when $A_1 \approx A_2$, because an infinite number of $P_1 = f_1^{-1}$ and $P_2 = f_2^{-1}$ period combinations can induce the observed period $P_3 = [(f_1 + f_2)/2]^{-1}$.

In Sect. 6.2, we noted that our $|\Delta\Omega|$ values in Table 4 may be underestimated. The P_{act} values of some stars published by Jetsu et al. (2017) are too close to P_{orb} , because they used *all* $t_{\text{min},1}$ values in their K-method analysis. *Had* they excluded the $t_{\text{min},1}$ values connected to the P_{orb} periodicity before their K-method analysis, some $|P_{\text{orb}} - P_{\text{act}}|$ differences would have been larger. Hence, we have underestimated the $|\Delta\Omega|$ values in our Table 4. In some cases, the K-method may even have detected only the P_{orb} periodicity, because P_{act} never dominated the observed light curve. This may have happened for example with DM UMA (Jetsu et al. 2017, Fig. 15a).

Regardless of the minima-incompatibility, the three migration alternatives MIGRATION₁, MIGRATION₂ and MIGRATION₃ do provide the *qualitative* answers to the *4th question*, the *5th question* and the *6th question*, which are given in PAPER II (Sect. 12).

There are other indirect ways to obtain less important additional information. Firstly, the ratio a_1/a_2 can be estimated from the range of $\phi_{\text{min},1}$ fluctuation (Eq. 47). Secondly, if the observed $s(t)$ light curve amplitude A_3 repeats some regular pattern, the amplitudes $A_1 = 2a_1$ and $A_2 = 2a_2$ can be solved from Eqs. 43 and 44. This gives

$$A_1 = (A_{3,\text{max}} - A_{3,\text{min}})/2 \quad (50)$$

$$A_2 = (A_{3,\text{max}} + A_{3,\text{min}})/23 \quad (51)$$

where $A_{3,\max}$ and $A_{3,\min}$ are the maximum and minimum values of the *observed* amplitude A_3 .

Although the number of possible $g_1(t)$ and $g_2(t)$ combinations is infinite, the above indirect approaches give us some hope of detecting the P_{act} and P_{rot} periodicities of FK Com. However, these indirect approaches rely on the assumption that the observed $s(t)$ light curve is a sum of two sinusoids. Even if this assumption were true, the interpretation of the observed light curves of FK Com would remain ambiguous, especially due to incompatibility. We have obtained *qualitative* answers to the *4th question*, the *5th question* and the *6th question*, but the *quantitative* estimates for the numerical values of P_{act} and P_{rot} are still missing. Hence, we are still at the dead encountered in Sect. 7.5.

8 DISCUSSION

Jetsu et al. (2017) presented the general light curve model for CABSSs and CASSs. This model was based on the JHL-argument. We define the complex 2P-model $g_C(t)$ and the simple 1P-model $g_S(t)$ in Sect. 3 (Eqs. 6 and 7).

The models of one-dimensional period finding methods, like the sinusoidal LS-model, have unique phases, and the shape of the light curve model does not change. These models can not describe the light curve of the 2P-model, because there are no unique phases for presenting the *observed* $g_C(t)$ light curve (Eq. 6). The shape of this $g_C(t)$ light curve is constantly changing. Therefore, the $g_C(t)$ light curve can be studied only as a function of time, not as a function of phase. The only unique phases are the ϕ_1 and ϕ_2 phases of the *real* $g_1(t)$ and $g_2(t)$ light curves (Eqs. 3 and 5).

The complex $g_C(t)$ model and the simple $g_S(t)$ model are nested (Sect. 3.3). They are the same model when $f_1 = f_2$ (CASE₁), and when $g_1(t)$ has $A_1 = 0$ (CASE₂) or $g_2(t)$ has $A_2 = 0$ (CASE₃). If none of these three cases occurs, we can compare the complex $g_C(t)$ model and the simple $g_S(t)$ model with the statistical criterion of Eq. 16, and choose which one is the better model for the data. Such comparisons will be done later in PAPER II (Sects. 2-4).

The earlier 2P-model analysis of thirteen CABSSs relied on the fixed P_{act} and $P_{\text{rot}} \approx P_{\text{orb}}$ values (Jetsu et al. 2017). One season of FK Com photometry was also studied with the 2P-model by first solving the fixed P_{act} value, and then solving the fixed P_{rot} value (Jetsu et al. 2017, Sect. 6.2).

In Sects. 5.1-5.2, we draw attention to the “sobering reminder” presented by Howard (1994), which may mean that all results obtained for the stellar SDR with the SI-method and the LC-method are not necessarily true, especially if the solar-stellar connection holds. Nevertheless, those earlier SDR results certainly contradict the JHL-argument (e.g. Strassmeier 2009, Sect. 7). For example, if this argument is true, the earlier SI-method studies should have detected the two constant periods P_{act} and $P_{\text{rot}} \approx P_{\text{orb}}$ of the JHL-argument (the *1st question*). We argue that the parameters $|k|$ (Eq. 18) and $|\Delta\Omega|$ (Eq. 19) of thirteen CABSSs in Table 4 support the idea that the earlier SI-method studies could have already detected these two periodicities. We also present *general* and *particular* evidence for this (Sects. 6.2 and 6.3). Long-lived starspots rotating with a constant angular velocity have been detected in many SI-method studies (e.g. Berdyugina et al. 1998;

Korhonen et al. 2000; Strassmeier & Bartus 2000). These results provide our answer to the *1st question*.

The LC-method gives several estimates for stellar SDR, like the $|k|$ or Z parameters (Eqs. 24, 25 and 28). The values of these parameters are computed from the observed changes of the photometric rotation period under the assumption that $P_{\text{phot}} \approx P_{\text{rot}}$ (Sect. 7.1). Numerous LC-method studies have confirmed that the stellar SDR decreases when P_{phot} decreases (Sect. 7.2). These $P_{\text{phot}} \approx P_{\text{rot}}$ changes in the observed light curves of CABSSs and CASSs contradict the JHL-argument (the *2nd question*).

The $P_{\text{phot}} \approx P_{\text{rot}}$ values have usually been determined with the one-dimensional period finding methods, like the LS-method. We simulate artificial data with the most simple 2P-model: the sum of two sinusoids (Sect. 7.3). These simulated data are analysed with the LS-method (Sect. 7.3.1-7.3.2). The results for the light curve periods (P_3), amplitudes (A_3) and minimum epochs ($t_{1,\min}$) reveal an effect that we refer to as “incompatibility” (Sect. 7.4). The observed values of all these three parameters change, although the underlying 2P-model does not change at all (Sects. 7.4.1-7.4.3). Due to this incompatibility effect, two observers *observing* the light curve of *same* star during the *same* time interval will get *different* P_3 , $|k|$ and Z estimates with the LS-method, or with any other one-dimensional period finding method. The incompatibility of the P_3 periods detected with the LS-method, or with any other one-dimensional period finding method, provides answers to the *2nd question* and the *3rd question*. This incompatibility effect does not only contaminate the LC-method results, because it can also mislead the identification of starspots in the surface images obtained with the SI-methods (Sect. 7.4.4).

Due to the minima-incompatibility effect, our study arrives at a dead end in Sect. 7.5. The K-method analysis of the minimum epochs $t_{\min,1}$ determined with the one-dimensional CPS-method does not give us an unambiguous P_{act} value for FK Com. The relation $P_{\text{rot}} \approx P_{\text{orb}}$ can not be used, because FK Com is not a binary. In other words, we have no *qualitative* or *quantitative* answers for the *4th question*, the *5th question* or the *6th question*.

The most simple 2P-model, the sum of two sinusoids, is already studied in Sect. 7.3. We show how the periods, the amplitudes and the minimum phases of this particular 2P-model can be solved analytically (Sect. 7.6). These solutions allow us to obtain indirect information of the *real* light curves (the two sinusoids) that cause the *observed* light curve (the sum of two sinusoids). For example, this indirect approach reveals the three migration alternatives MIGRATION₁, MIGRATION₂ and MIGRATION₃ (Sect. 7.7). These migration alternatives provide *qualitative* answers to the *4th question*, the *5th question* and the *6th question*. For example, perfect flip-flop events $\Delta\phi_b = 0.5$ occur when the two real light curves are equal amplitude sinusoids (Eq. 48).

The above indirect solutions are valid *only*, if the correct complex $g_C(t)$ model is a sum of two sinusoids. In this case, the sum curve $g_C(t)$ is also a sinusoid (Eqs. 37 and 40). For example, if the *observed* $g_C(t)$ light curve has two minima, then at least one of the real $g_1(t)$ and $g_2(t)$ light curves can not be a sinusoid. In this case, the analytical relations for a sum of sinusoids given in Sect. 7.6 are no longer valid. Thus, the *quantitative* answers to the *4th question* and the *5th question* are still missing. The only way out of this

dead end is to formulate a new two-dimensional period analysis method, which gives the unambiguous solutions for all parameters of the 2P-model. This is done in PAPER II.

9 CONCLUSIONS

In this first paper, we study the real and the simulated photometry of FK Com to verify validity of the following argument made by Jetsu et al. (2017):

- JHL-argument: “The *observed* light curves of chromospherically active binary and single stars are interference of two *real* constant period light curves of long-lived starspots. These constant periods are the non-stationary active longitude period P_{act} and the stationary rotation period $P_{\text{rot}} \approx P_{\text{orb}}$.”

This argument is not supported by the current widely held views of the stellar surface differential rotation and the starspots (e.g. Strassmeier 2009, Sect. 7). Therefore, we make six specific questions which undermine this argument (Sect. 1). Our aim is to answer all these questions.

We present general and particular evidence that the long-lived starspots predicted by the JHL-argument have already been detected in the earlier SI-method studies. Our LS-method analysis of the real and the simulated photometry of FK Com reveals that the results obtained with *any* one-dimensional period analysis method suffer from incompatibility. *If* the JHL-argument is true, the one-dimensional period finding methods, like the LS-method, detect spurious period, amplitude and minimum epoch estimates from the observed light curves. These spurious estimates have nothing to do with the real periods, the real amplitudes and the real minimum epochs of the two real light curves of the JHL-argument. This would mean that all earlier one-dimensional period analysis studies of the light curves of chromospherically active stars have given spurious results since the starspots were discovered by Kron (1947). The spurious period changes detected with these LC-methods would explain why the light curves and the surface images give different surface SDR estimates even for the same star. We also show that it is possible to obtain indirect information of the two *real* light curves, if the *observed* light curve is a sum of two constant period sinusoids.

In conclusion, *if* the JHL-argument is true, we can already answer the *1st question*, the *2nd question*, the *3rd question* and the *6th question*. We can also give *qualitative* answers to the *4th question* and the *5th question*. Even if the JHL-argument were true, the *quantitative* answers to the *4th question* and the *5th question* are still missing, because we can not solve the unambiguous values for the P_{act} and P_{rot} periods of FK Com. Hence, our study arrives at a dead end, because we can not prove that the long-lived starspots predicted by the JHL-argument do exist in FK Com. We solve this problem in our second paper, where we formulate a new two-dimensional period finding method, solve the real light curves of FK Com and determine its unambiguous P_{act} and P_{rot} period values. The compact answers to all the above mentioned six specific questions are given in PAPER II (Sect. 12).

ACKNOWLEDGEMENTS

We thank Thomas Hackman and Ilana Hilesmaa for their comments of this manuscript. This work has made use of NASA’s Astrophysics Data System (ADS) services.

REFERENCES

- Balona L. A., Abedigamba O. P., 2016, *MNRAS*, **461**, 497
 Barnes J. R., Collier Cameron A., Donati J.-F., James D. J., Marsden S. C., Petit P., 2005, *MNRAS*, **357**, L1
 Berdyugina S. V., Berdyugin A. V., Ilyin I., Tuominen I., 1998, *A&A*, **340**, 437
 Bopp B. W., Stencel R. E., 1981, *ApJ*, **247**, L131
 Chugainov P. F., 1966, Information Bulletin on Variable Stars, **172**
 Cole E. M., Hackman T., Käpylä M. J., Ilyin I., Kochukhov O., Piskunov N., 2015, *A&A*, **581**, A69
 Collier Cameron A., 2007, *Astronomische Nachrichten*, **328**, 1030
 Distefano E., Lanzafame A. C., Lanza A. F., Messina S., Spada F., 2016, *A&A*, **591**, A43
 Draper N. R., Smith H., 1998, Applied Regression Analysis. John Wiley & Sons, Inc., doi:10.1002/9781118625590
 Eggen O. J., Iben Jr. I., 1989, *AJ*, **97**, 431
 Hackman T., 2004, PhD thesis, University of Helsinki, Finland
 Hackman T., et al., 2013, *A&A*, **553**, A40
 Hale G. E., 1908, *ApJ*, **28**, 315
 Hall D. S., 1991, in Tuominen I., Moss D., Rüdiger G., eds, Lecture Notes in Physics, Berlin Springer Verlag Vol. 380, IAU Colloq. 130: The Sun and Cool Stars. Activity, Magnetism, Dynamism. p. 353, doi:10.1007/3-540-53955-7_156
 Hall D. S., Busby M. R., 1990, in NATO Advanced Science Institutes (ASI) Series C. p. 377
 Henry G. W., 1995, in Henry G. W., Eaton J. A., eds, Astronomical Society of the Pacific Conference Series Vol. 79, Robotic Telescopes. Current Capabilities, Present Developments, and Future Prospects for Automated Astronomy. p. 44
 Howard R. F., 1994, in Balasubramaniam K. S., Simon G. W., eds, Astronomical Society of the Pacific Conference Series Vol. 68, Solar Active Region Evolution: Comparing Models with Observations. p. 1
 Howell S. B., Mason E., Boyd P., Smith K. L., Gelino D. M., 2016, *ApJ*, **831**, 27
 Jetsu L., 1996, *A&A*, **314**, 153
 Jetsu L., 2018, *MNRAS* (PAPER II: submitted)
 Jetsu L., Pelt J., 1999, *A&AS*, **139**, 629
 Jetsu L., Porceddu S., 2015, *PLoS ONE*, **10**(12), e0144140
 Jetsu L., Pelt J., Tuominen I., Nations H., 1991, in Tuominen I., Moss D., Rüdiger G., eds, Lecture Notes in Physics, Berlin Springer Verlag Vol. 380, IAU Colloq. 130: The Sun and Cool Stars. Activity, Magnetism, Dynamism. p. 381, doi:10.1007/3-540-53955-7_161
 Jetsu L., Pelt J., Tuominen I., 1993, *A&A*, **278**, 449
 Jetsu L., Pelt J., Tuominen I., 1999, *A&A*, **351**, 212
 Jetsu L., Hackman T., Hall D. S., Henry G. W., Kokko M., You J., 2000, *A&A*, **362**, 223
 Jetsu L., Porceddu S., Lyytinen J., Kajatkari P., Lehtinen J., Markkanen T., Toivari-Viitala J., 2013, *ApJ*, **773**, 1
 Jetsu L., Henry G. W., Lehtinen J., 2017, *ApJ*, **838**, 122
 Kóvári Z., Oláh K., Kriskovics L., Vida K., Forgács-Dajka E., Strassmeier K. G., 2017, *Astronomische Nachrichten*, **338**, 903
 Kochukhov O., 2016, in Rozelot J.-P., Neiner C., eds, Lecture Notes in Physics, Berlin Springer Verlag Vol. 914, Lecture Notes in Physics, Berlin Springer Verlag. p. 177, doi:10.1007/978-3-319-24151-7_9

Korhonen H., Berdyugina S. V., Hackman T., Duemmler R., Ilyin I. V., Tuominen I., 1999, *A&A*, **346**, 101

Korhonen H., Berdyugina S. V., Hackman T., Strassmeier K. G., Tuominen I., 2000, *A&A*, **360**, 1067

Korhonen H., Berdyugina S. V., Tuominen I., 2002, *A&A*, **390**, 179

Korhonen H., Berdyugina S. V., Tuominen I., 2004, *Astronomische Nachrichten*, **325**, 402

Korhonen H., Berdyugina S. V., Hackman T., Ilyin I. V., Strassmeier K. G., Tuominen I., 2007, *A&A*, **476**, 881

Korhonen H., Berdyugina S. V., Ilyin I. V., Strassmeier K. G., Hackman T., 2009, in *Revista Mexicana de Astronomia y Astrofisica Conference Series*. pp CD323–CD327

Kron G. E., 1947, *PASP*, **59**, 261

Lehtinen J., Jetsu L., Hackman T., Kajatkari P., Henry G. W., 2011, *A&A*, **527**, A136

Lehtinen J., Jetsu L., Hackman T., Kajatkari P., Henry G. W., 2012, *A&A*, **542**, A38

Lehtinen J., Jetsu L., Hackman T., Kajatkari P., Henry G. W., 2016, *A&A*, **588**, A38

Lindborg M., Korpi M. J., Hackman T., Tuominen I., Ilyin I., Piskunov N., 2011, *A&A*, **526**, A44

Lomb N. R., 1976, *Ap&SS*, **39**, 447

Oláh K., Korhonen H., Kóvári Z., Forgács-Dajka E., Strassmeier K. G., 2006, *A&A*, **452**, 303

Panov K., Dimitrov D., 2007, *A&A*, **467**, 229

Petit P., et al., 2004, *MNRAS*, **351**, 826

Porceddu S., Jetsu L., Markkanen T., Toivari-Viitala J., 2008, *Cambridge Archaeological Journal*, **18**, 327

Porceddu S., Jetsu L., Markkanen T., Lyytinen J., Kajatkari P., Lehtinen J., Toivari-Viitala J., 2018, *Open Astronomy*, **27**, 232

Puzin V. B., Savanov I. S., Dmitrienko E. S., 2014, *Astronomy Reports*, **58**, 471

Puzin V. B., Savanov I. S., Dmitrienko E. S., 2017, *Astronomy Reports*, **61**, 693

Radick R. R., Lockwood G. W., Henry G. W., Hall J. C., Pevtsov A. A., 2018, *ApJ*, **855**, 75

Reinhold T., Gizon L., 2015, *A&A*, **583**, A65

Reinhold T., Reiners A., 2013, *A&A*, **557**, A11

Reinhold T., Reiners A., Basri G., 2013, *A&A*, **560**, A4

Scargle J. D., 1982, *ApJ*, **263**, 835

Schwabe M., 1844, *Astronomische Nachrichten*, **21**, 233

Strassmeier K. G., 2009, *A&ARv*, **17**, 251

Strassmeier K. G., 2011, in Prasad Choudhary D., Strassmeier K. G., eds, *IAU Symposium Vol. 273, Physics of Sun and Star Spots*. pp 174–180, doi:10.1017/S1743921311015201

Strassmeier K. G., Bartus J., 2000, *A&A*, **354**, 537

Strassmeier K. G., Boyd L. J., Epan D. H., Granzer T., 1997, *PASP*, **109**, 697

Van Helden A., 1996, *Proc. Am. Phil. Soc.*, **140**, 358

Vida K., Korhonen H., Ilyin I. V., Oláh K., Andersen M. I., Hackman T., 2015, *A&A*, **580**, A64

Washuettl A., Strassmeier K. G., Weber M., 2009, *Astronomische Nachrichten*, **330**, 366

Webbink R. F., 1976, *ApJ*, **209**, 829

Welty A. D., Ramsey L. W., 1994, *ApJ*, **435**, 848

Willson R. C., Hudson H. S., 1991, *Nature*, **351**, 42

- CASS: Chromospherically Active Single Star (PAPER I: Sect. 1)
- SDR: Surface Differential Rotation (PAPER I: Sect. 1)
- JHL-argument: Jetsu et al. (2017) argument (PAPER I: Sect. 1)
- SI-method: Surface Images measure SDR (PAPER I: Sect. 1)
- LC-method: Light Curves measure SDR (PAPER I: Sect. 1)
- TEL=1: T7 telescope photometry (PAPER I: Sect. 2)
- TEL=2: Ph10 telescope photometry (PAPER I: Sect. 2)
- SEG: Data segment number (PAPER I: Sect. 2)
- CPS-method: Continuous Period Search method (PAPER I: Sect. 2)
- CPS-model: Continuous Period Search model (PAPER I: Sect. 2)
- DATA_{x,y}: TEL=x data of SEG=y (PAPER I: Sect. 3)
- 2P-model: Two Period model (PAPER I: Sect. 3.1)
- 1P-model: One Period model (PAPER I: Sect. 3.2)
- LS-method: Lomb-Scargle method (PAPER I: Sect. 7)
- LS-model: Lomb-Scargle model (PAPER I: Sect. 7)
- TEST_{a₁=a₂}: 2P-model test $A_1 = A_2$ (PAPER I: Sect. 7.3.1)
- TEST_{a₁<a₂}: 2P-model test $A_1 < A_2$ (PAPER I: Sect. 7.3.2)
- 2P-method: Two period method (PAPER II: Sect. 2.1)
- 1P-method: One period method (PAPER II: Sect. 2.2)
- WK-method: Weighted Kuiper method (PAPER II: Sect. 7)

We introduce these abbreviations in the sections given above in the parenthesis. For easy readability, we do not use these abbreviations in our six specific questions or in our answers to these six questions, except for the JHL-argument abbreviation.

This paper has been typeset from a $\text{\TeX}/\text{\LaTeX}$ file prepared by the author.

APPENDIX A: ABBREVIATIONS

We use the following abbreviations in PAPER I and PAPER II

- K-method: Kuiper method (PAPER I: Sect. 1)
- CABS: Chromospherically Active Binary Star (PAPER I: Sect. 1)
- MLC: Mean Light Curve (PAPER I: Sect. 1)